5

"Coseismic Foliations" in Gouge and Cataclasite: Experimental Observations and Consequences for Interpreting the Fault Rock Record

Steven A. F. Smith[1], James R. Griffiths[1], Michele Fondriest[2], and Giulio Di Toro[2,3,4]

ABSTRACT

Foliated gouges and cataclasites are commonly interpreted as the product of distributed (aseismic) fault creep. However, foliated fault rocks are often associated with localized slip surfaces, the latter indicating potentially unstable (seismic) behavior. One possibility is that such fault zones preserve the effects of both seismic slip and slower aseismic creep. An alternative possibility explored here is that some foliated fault rocks and localized slip surfaces develop contemporaneously during seismic slip. We studied the microstructural evolution of calcite-dolomite gouges deformed experimentally at slip velocities <1.13 m s^{-1} and for total displacements of 0.03–1 m, in the range expected for the average coseismic slip during earthquakes of Mw 3–7. As strain progressively localized in the gouge layers at the onset of high-velocity shearing, an initial mixed assemblage of calcite and dolomite grains evolved quickly to an organized, foliated fabric. The foliation was defined mainly by compositional layering and grain size variations that formed by cataclasis and shearing of individual foliation domains. The most significant microstructural changes in the bulk gouge occurred before and during dynamic weakening (<0.08 m displacement). Strain was localized to a bounding slip surface by the end of dynamic weakening, and thus microstructural evolution in the bulk gouge ceased. Our experiments suggest that certain types of foliated gouge and cataclasite can form by distributed brittle "flow" as strain localizes to a bounding slip surface during coseismic shearing.

5.1. INTRODUCTION

Foliated gouges and cataclasites are among the most common products of mid- to upper-crustal faulting [*Engelder*, 1974; *Chester et al.*, 1985]. In active and exhumed fault zones, the structure of foliated gouges and cataclasites is commonly used to determine the shear sense and kinematics of faulting, as well as the strain distribution in deformed fault rocks [e.g., *Rutter et al.*, 1986; *Chester and Logan*, 1987; *Tanaka*, 1992; *Cowan and Brandon*, 1994; *Cladouhos*, 1999; *Lin*, 2001; *Cowan et al.*, 2003; *Collettini and Holdsworth,* 2004; *Hayman et al.*, 2004]. Interpreting the significance and possible mechanical behavior of fault rocks in the geological record requires a complete understanding of the nature and evolution of fault rock foliations.

In natural gouges and cataclasites, foliation can be defined by a wide range of fabric elements and

[1] *Department of Geology, University of Otago, Dunedin, New Zealand*

[2] *School of Earth, Atmospheric and Environmental Sciences, University of Manchester, Manchester, UK*

[3] *Dipartimento di Geoscienze, Università degli Studi di Padova, Italy*

[4] *Istituto Nazionale di Geofisica e Vulcanologia, Rome, Italy*

Fault Zone Dynamic Processes: Evolution of Fault Properties During Seismic Rupture, Geophysical Monograph 227, First Edition. Edited by Marion Y. Thomas, Thomas M. Mitchell, and Harsha S. Bhat.

microstructures that reflect competition between brittle, plastic, and fluid-mediated deformation processes [*Snoke et al.*, 1998]. Microstructures that commonly contribute to foliations include compositional layering; particle size variations; preferred alignment of grains, grain boundaries, and fractures; and the orientation and connectivity of shear surfaces and dissolution surfaces. Foliations are commonly found in conjunction with discrete slip surfaces that indicate relatively localized deformation.

Where natural foliated gouges and cataclasites contain networks and overgrowths of phyllosilicate minerals, a convincing argument has been made that the phyllosilicate-rich foliations are formed by a combination of frictional sliding and dissolution-precipitation reactions, perhaps during aseismic fault creep [e.g., *Wintsch et al.*, 1995; *Imber et al.*, 1997; *Manatschal*, 1999; *Stewart et al.*, 2000; *White*, 2001; *Wintsch and Yi*, 2002; *Gueydan et al.*, 2003; *Collettini and Holdsworth*, 2004; *Holdsworth*, 2004; *Jefferies et al.*, 2006; *Moore and Rymer*, 2007; *Collettini et al.*, 2009; *Holdsworth et al.*, 2011; *Wallis et al.*, 2013; *Wallis et al.*, 2015]. *Bos et al.* [2000] and *Niemeijer and Spiers* [2006] provided experimental data in support of this interpretation by demonstrating that well-defined fault rock foliations can form by efficient dissolution-precipitation reactions accompanying granular flow and frictional sliding at low slip velocities ($<1\,\mu m\,s^{-1}$).

In other types of foliated fault rock, but particularly those in which cataclastic deformation is expected to dominate, Cowan [1999] argued that there is no compelling field or experimental evidence to rule out the possibility that foliations may form by distributed brittle "flow" during seismic slip. This alternative idea for the genesis of some foliated fault rocks has received little attention, despite the important consequences it has for interpreting the fault rock record. Experimental studies involving high-velocity ($V > 0.01\,m\,s^{-1}$) shearing of gouge layers allow for the investigation of microstructure evolution under conditions approaching the seismic range [*Niemeijer et al.*, 2012]. In several recent studies, high-velocity shearing was associated with the development of a foliated or banded microstructure in gouge layers, interpreted to reflect rotation of platy minerals during shear [e.g., *Kitajima et al.*, 2010] or particle welding driven by frictional heating [e.g., *Sawai et al.*, 2012; *Togo and Shimamoto*, 2012, *Yao et al.*, 2013].

As part of a wider study into the mechanical behavior of mixed (multiphase) gouges, we performed a series of experiments on calcite-dolomite gouges at seismic slip rates ($V_{max} < 1.13$ m/s). Calcite and dolomite are dominant minerals in many seismically active regions worldwide, where earthquake ruptures nucleate within and propagate through thick sequences of carbonates (e.g., Italy, 2009 Mw 6.3 L'Aquila earthquake; Greece, 1995 Ms 6.6 Western Macedonia earthquake). The ability to apply moderately high normal stresses (17.3 MPa) to the experimental gouge layers and precisely control the total displacements allowed us to investigate gouge microstructure and grain size evolution in the range of displacements (0.03–1 m; Table 5.1) expected for earthquakes of approximately magnitude Mw 3–7 [*Stirling et al.*, 2013]. The overall aim of the experiments was to explore the idea put forward by *Cowan* [1999] that some types of foliated gouge and cataclasite could form at seismic slip rates.

5.2. METHODS

5.2.1. Starting Materials and Gouge Sample Preparation

Gouges were prepared from mixtures of 50 wt% calcite and 50 wt% dolomite. The calcite component was derived by crushing Carrara marble, composed of >98 wt% calcite with <2 wt% dolomite and muscovite (from X-ray powder diffraction analysis). Original metamorphic grains in the Carrara marble are large, equant grains 150–400 μm in size. The dolomite component was derived by crushing sedimentary dolostones of the Mendola Formation of northeast Italy, a mid-Triassic unit 250–300 m thick [*Fondriest et al.*, 2015]. The Mendola Formation contains a matrix of micritic dolomite grains up to 10 μm in size as well as elongate (approximately bedding-parallel) fenestrae that are filled with rhombohedral dolomite crystals up to 300 μm long [*Fondriest et al.*, 2015].

Fragments of Carrara marble and Mendola Formation were crushed using a pestle and mortar, and the resulting material was passed through a 250-μm sieve. All material that passed through the sieve was retained for the experimental gouge mixes. The calcite and dolomite components were weighed and mixed by slow tumbling for up to 1 hour to ensure a homogenous distribution of phases. X-ray powder diffraction analysis performed on the mixed gouges indicated a composition of 44.7 wt% calcite and 55.3 wt% dolomite (±2–3 wt%) with no detectable accessory phases.

5.2.2. Experimental Procedures

Experiments were performed with SHIVA (**S**low- to **Hi**gh-**V**elocity rotary-shear friction **A**pparatus) at the INGV, Rome [*Di Toro et al.*, 2010; *Niemeijer et al.*, 2011] using a sample holder for incohesive materials with rotary and stationary parts (Figure 5.1a) [*Smith et al.*, 2013]. The rotary base plate and the stationary base disc have a crosshatch pattern of surface roughness where they are

Table 5.1 Summary of experiments performed on mixed calcite-dolomite gouges (50 wt%/50 wt%) with increasing displacements. See text for explanation of grain size measurements and units 1–3.

Exp.	Normal Stress (MPa)	[a]Max. Slip Vel. ($m\,s^{-1}$)	Displacement (m)	[b]Bulk shear strain, γ	Mean grain size calcite (d_{equ}, μm)	Mean grain size dolomite (d_{equ}, μm)	Max. grain size calcite (d_{equ}, μm)	Max. grain size dolomite (d_{equ}, μm)	Unit 1 (%)	Unit 2 (%)	Unit 3 (%)
s800	17.3	–	–	–	6.4, 5.9[c]	5.6	107.3, 45.88[c]	55.4	—	—	—
s796	17.3	0.4	0.03	15	2.9	5.5	48.2	33.5	95.1	4.9	0.0
s801	17.3	0.56	0.05	25	3.7	5.3	21.9	24.9	73.6	26.2	0.2
s797	17.3	0.76	0.08	40	2.1	3.8	13.8	22.8	67.9	32.0	0.1
s798	17.3	1.13	0.19	95	1.9	4.1	15.3	28.3	55.4	43.9	0.7
s799	17.3	1.13	0.39	195	2.9	4.5	21.2	20.4	44.8	49.0	6.2
s530	17.3	1.13	0.99	495	—	—	—	—	—	—	—

[a] Target slip velocity in all experiments was $1.13\,m\,s^{-1}$, but this velocity was not obtained in the three shortest displacement experiments (see Figure 5.3). All experiments had the same acceleration and deceleration of $7\,m\,s^{-2}$.
[b] Calculated as total displacement divided by measured final thickness of gouge layer.
[c] First number includes largest measured clast, second number exludes largest measured clast.

in contact with the gouge layer (Figure 5.1c; amplitude of surface roughness 200 μm, wavelength 400 μm). Normal load on the gouge layer is applied by the axial loading column of SHIVA [*Di Toro et al.,* 2010]. Normal load on the inner and outer sliding rings is modulated by five outer springs and one inner spring (Figure 5.1a). Each experiment used 3 g of gouge, resulting in a ring-shaped gouge layer (Figure 5.1b; 55 mm/35 mm ext./int. diameter) with an initial (precompaction) thickness of c. 2 mm.

Experiments were performed under room-dry conditions (room humidity varied between 50% and 80%) at a constant normal stress of 17.3 MPa and target maximum slip velocity of $1.13\,m\,s^{-1}$ (Table 5.1). Angular rotation (and total displacement) in each experiment was controlled using two digital optical encoders located on the rotary column [*Di Toro et al.*, 2010; *Niemeijer et al.*, 2011]. Horizontal displacements of the axial column were measured using a direct current differential transformer (50 mm range and ~ 50 μm resolution) and in some experiments a linear variable differential transformer (3 mm range and ~ 0.03 μm resolution). Experimental data (e.g., axial load, torque, axial displacements, angular rotation) were acquired at a frequency up to 25 kHz, and determination of total displacement, slip rate, and shear stress followed methods outlined in *Di Toro et al.* [2010].

5.2.3. Microstructural Analysis

Quantitatively comparing the microstructure of two-phase gouges deformed in separate high-velocity experiments requires confidence that the starting materials in each experiment were nearly identical, and that the gouge sample assembly and experimental conditions remained the same. In our experience, minor variations to any of these factors can result in changes to the final microstructure. For this reason, quantitative microstructural analysis (e.g., shear strain, grain size) presented in this chapter focuses on six experiments (one compaction experiment and five shear experiments) performed consecutively (on the same day) using gouge material from the same batch and with an identical sample assembly (Table 5.1). The five shear experiments had displacements in the range of 0.03–0.39 m (Table 5.1). We supplement these with an additional experiment (s530) with 1 m of displacement (Table 5.1). Because experiment s530 was performed with a different batch of starting gouge and a slightly modified sample holder, we found that aspects of the microstructure of this experiment (e.g., mean grain sizes, unit thicknesses; described below) were not directly comparable to the other five shear experiments. However, we use s530 in a qualitative way to illustrate general characteristics of the gouge fabric at relatively large displacements.

Fragments of deformed gouge layers were impregnated under vacuum using low-viscosity epoxy. Polished petrographic sections cut perpendicular to the gouge layers and approximately parallel to the slip direction (Figure 5.1b) were prepared for microstructural observations using a transmitted-light microscope and a Zeiss Sigma VP field-emission scanning electron microscope (SEM; in the Otago Centre for Electron Microscopy, University of Otago) operating in backscattered mode (acquisition conditions: accelerating voltage 15 kV,

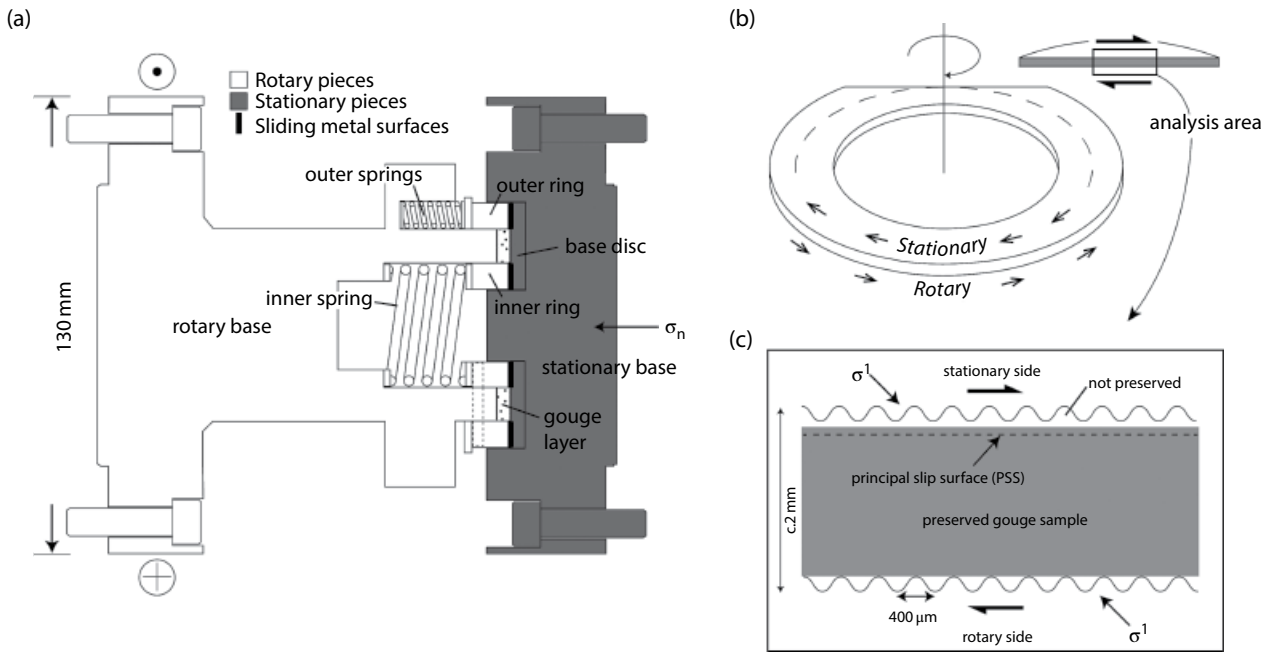

Figure 5.1 Gouge sample holder and experimental setup. (a) Scale diagram of gouge holder with main parts labeled. (b) Geometry of the annular gouge layer. Thin sections were prepared perpendicular to gouge layer boundaries and approximately parallel to the sliding direction. The central part of each thin section (box labeled "analysis area") was used for microstructural analysis. (c) Enlargement of the analysis area showing gouge layer boundaries. The gouge layer in each experiment was c. 2 mm thick prior to compaction. Where in contact with the gouge layer, the rotary and stationary pieces have surface roughness with wavelength of 400 µm and amplitude of 200 µm. The dashed line indicates the region where the principal slip surface (PSS) develops in the gouge layers. After the experiments, the gouge layers were quite cohesive and split close to the PSS. The grey area is typically preserved for microstructural analysis.

working distance 6–8.5 mm). Energy-dispersive X-ray spectroscopy (EDS) on the SEM was used to produce element maps showing the distribution of calcite (relatively enriched in calcium) and dolomite (relatively enriched in magnesium).

Microstructure and grain size in the starting materials and deformed samples were analyzed using quantitative image analysis techniques described in the sections that follow. To minimize potential errors associated with comparing the microstructure of different samples, petrographic sections were cut along the tangent to a circle lying between the inner and outer diameters of the ring-shaped gouge layer (dashed ring in Figure 5.1b). Quantitative microstructural analysis was performed on the central parts of the thin sections where the plane of the thin section is approximately parallel to the slip direction (Figures 5.1b, c).

Deformed gouge layers often split during sample preservation. A schematic indication of the gouge material that was typically preserved during sample recovery is shown in Figure 5.1c (grey area is preserved). The preserved area includes the bulk of the gouge layer, the localized principal slip surface that forms during shearing, and also a thin sliver (up to 200 µm) of cohesive material on the stationary side of the principal slip surface.

5.3. RESULTS

5.3.1. Starting Gouge Microstructure

Figure 5.2a shows a SEM image of the calcite-dolomite starting gouge compacted to 17.3 MPa normal stress (the same normal stress used in the shear experiments). Calcite grains are mainly single-crystal grains, consistent with their derivation from large metamorphic grains in the Carrara marble. Dolomite grains are either single-crystal or polycrystalline (Figure 5.2b). The single-crystal dolomite grains are derived from the large rhombohedral dolomite crystals filling the fenestrae in the Mendola Formation. The polycrystalline grains are derived from the finer-grained micritic matrix of the Mendola Formation, which consists of regions with a granular (e.g., grain on left side in Figure 5.2b) or more crystalline (e.g., grain on right side in Figure 5.2b) texture. Calcite in

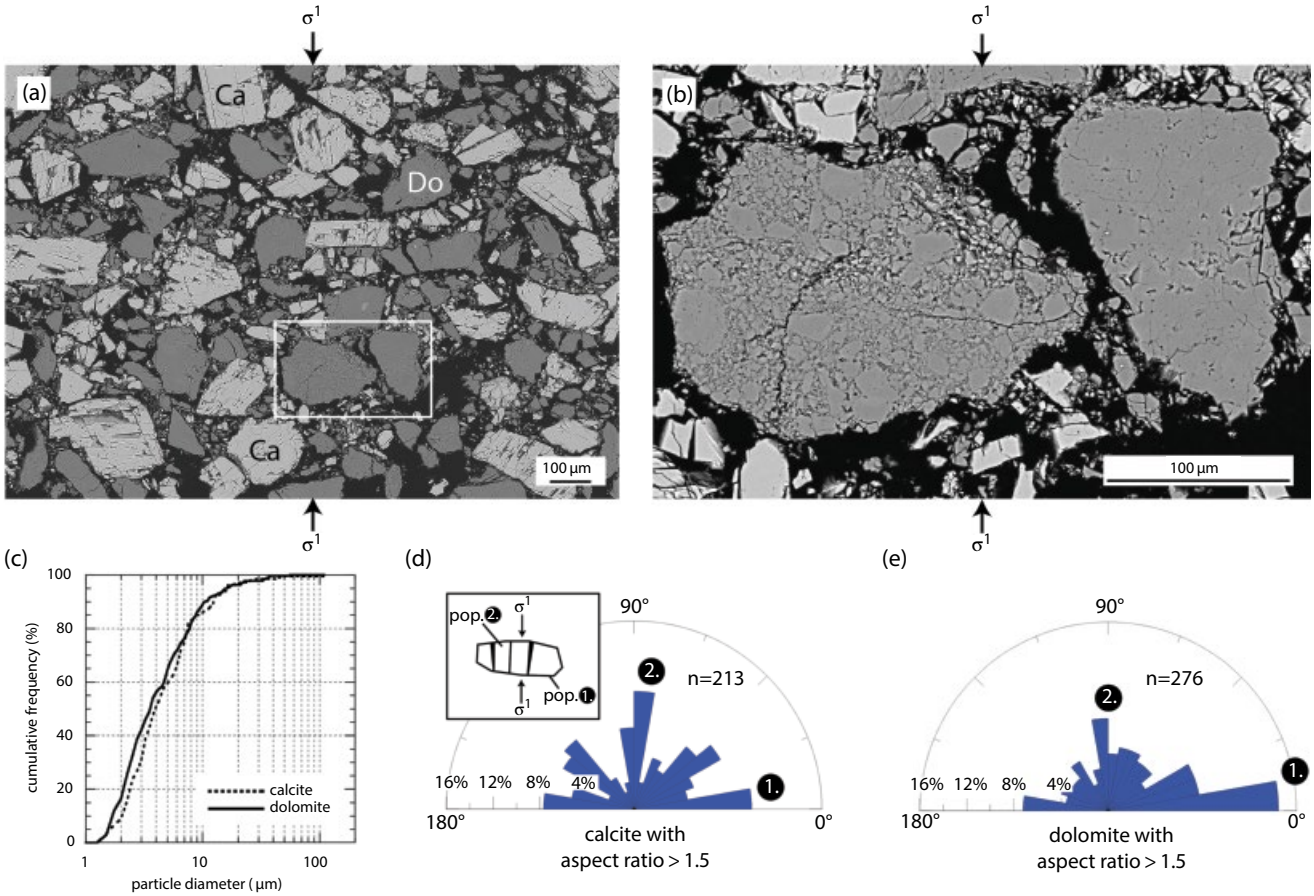

Figure 5.2 Characterization of gouge starting materials. (a) Scanning electron microscope (SEM) image of mixed calcite-dolomite gouges compacted to 17.3 MPa normal stress. Ca = calcite; Do = dolomite. Thin section was prepared with the same orientation as for the shear experiments (Figure 5.1b, c). Arrows indicate orientation of compaction (σ^1). Calcite and dolomite grains appear homogenously mixed and are extensively fractured during compaction. (b) Enlargement of two dolomite grains shown in part a. The dolomite grain on the right is a polycrystalline grain consisting of tightly interlocking polygonal dolomite crystals, derived from the relatively coarse-grained dolomite veins or fenestrae-filling dolomite crystals in the starting rock (Mendola Formation). The dolomite grain on the left is an aggregate of subrounded grains bound together by a fine-grained (<5 µm) matrix. This type of polycrystalline dolomite grain is derived from the micritic matrix of the Mendola Formation. (c) Particle size distribution of gouge starting materials compacted to 17.3 MPa normal stress. Particle sizes were calculated from image analysis methods described in section 5.3.3.5. (d) Rose diagram summarizing the orientations of elongate (aspect ratio of best-fit ellipses >1.5) calcite grains. The inset cartoon shows an interpretation of main populations 1 and 2. (e) Rose diagram summarizing the orientations of elongate (aspect ratio of best-fit ellipses >1.5) dolomite grains.

the compacted starting material is twinned, although no twin preferred orientation was noted. Both calcite and dolomite grains are also heavily fractured Figure 5.2a), particularly along twin and cleavage planes.

Image analysis (described in section 5.3.3.5) indicates that the grain size distributions of calcite and dolomite in the starting material are similar (Figure 5.2c), although calcite has a slightly larger mean grain size (6.37 µm) than dolomite (5.65 µm). Approximately 60% of calcite and dolomite grains in the starting material have aspect ratios (long axis of best-fit ellipse/short axis of best-fit ellipse; see section 5.3.3.5) greater than 1.5. These elongate grains show a range of preferred orientations (Figure 5.2d, e). In both calcite and dolomite there is a population of grains (pop. 1 in Figure 5.2d, e) with long axes oriented subparallel to gouge layer boundaries (i.e., subperpendicular to the compaction direction, σ1). Grains of this population commonly fracture at high angles to their long axes during compaction (see inset Figure 5.2d), producing a second population of elongate grains (pop. 2 in Figure 5.2d, e) with long axes oriented subparallel to the compression direction. Calcite in the starting materials shows two

additional populations of elongate grains with long axes oriented obliquely to the compaction direction (Figure 5.2d).

5.3.2. Mechanical Data

The five shear experiments used for quantitative microstructural analysis were performed under identical conditions of normal stress (17.3 MPa) and slip velocity but with increasing displacements in the range of 0.03–0. 39 m (Figure 5.3a). The target maximum slip velocity was 1.13 m s^{-1}. Acceleration and deceleration in each experiment were 7 m s^{-2}, meaning that only the two highest-displacement experiments reached the target slip velocity (Figure 5.3b).

An initial phase of transient strengthening occurred in the experiments before peak shear stress was reached after c. 0.02 m displacement (Figure 5.3a). Peak shear stress of c. 12 MPa corresponds to a friction coefficient (μ = shear stress/normal stress) of 0.7. Peak stress was followed by rapid dynamic weakening to reach (in the two experiments with the largest displacements) a much lower shear stress value of c. 4 MPa, corresponding to μ of 0.25 (Figure 5.3a). The onset of dynamic weakening occurred at a slip velocity of c. 0.5 m s^{-1} (Figure 5.3b). The phase of rapid dynamic weakening was over by c. 0.08 m displacement (Figure 5.3a) as shear stress transitioned to "steady-state" values (only achieved in the experiment with 0.39 m displacement). During deceleration at the end of the experiments, shear stress recovered to c. 9.5 MPa (corresponding to μ of 0.55; Figure 5.3a).

Experiments showed an initial phase of rapid axial shortening followed by more gradual shortening with increasing displacement (Figure 5.3a). Inspection of the sliding rings after disassembly of the sample holder suggests that no gouge loss occurred during most of the experiments, and thus axial shortening is interpreted to represent gouge compaction during shearing. The exception to this is the experiment with 0.05 m displacement that showed anomalous amounts of shortening at the onset of slip (Figure 5.3a). Minor gouge loss may have occurred during this experiment.

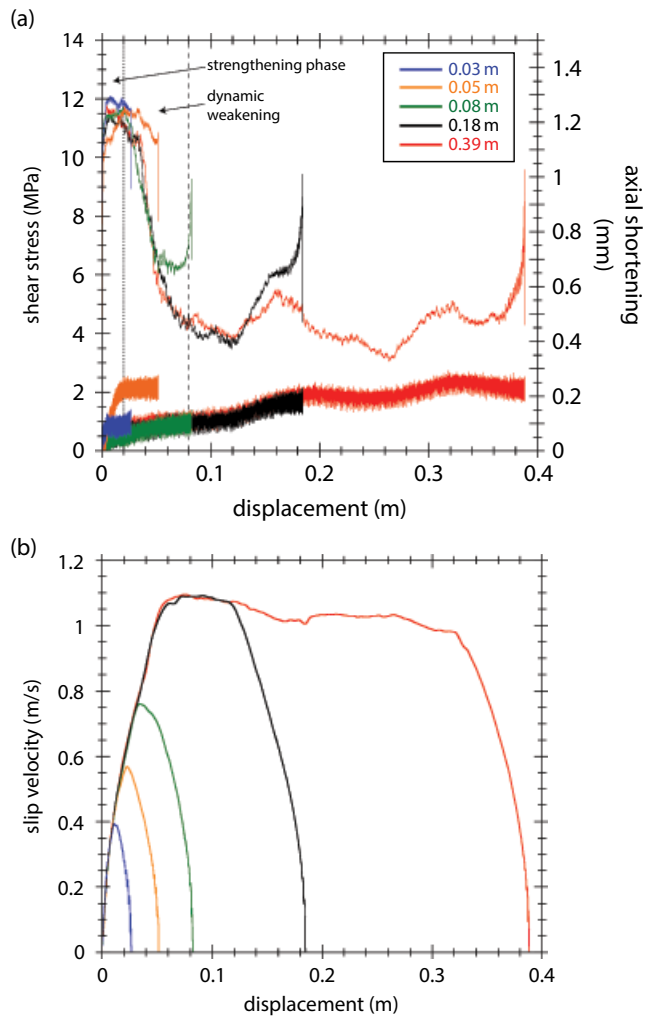

Figure 5.3 Mechanical data. (a) Shear stress and axial shortening vs. displacement. All experiments showed an initial strengthening phase before peak stress (c. 12 MPa) was reached after c. 0.02 m of slip. Dynamic weakening occurred between c. 0.02 and 0.08 m. The two experiments with the largest displacements (0.18 m and 0.39 m) had a minimum shear stress value of approximately 4 MPa. Axial shortening followed a similar trend in all experiments, with total shortening of c. 0.2 mm after 0.39 m of slip. The experiment with 0.05 m displacement showed anomalously large amounts of shortening that probably reflects minor gouge loss. (b) Slip velocity vs. displacement for the same five experiments shown in part a. Acceleration and deceleration were 7 m s^{-2}. *See electronic version for color representation.*

5.3.3. Deformed Gouge Microstructure

5.3.3.1. Foliation Development and Microstructural Units

As observed in previous high-velocity gouge experiments on carbonates [*De Paola et al.*, 2011; *Fondriest et al.*, 2013; *Smith et al.*, 2013; *Ree et al.*, 2014; *Bullock et al.*, 2015; *Smith et al.*, 2015) and other rock types [e.g., *Brantut et al.*, 2008; *Kitajima et al.*, 2010; *Oohashi et al.*, 2011; *Proctor et al.*, 2014], shearing of the mixed calcite-dolomite gouge layers was associated with the progressive development of a discrete principal slip surface (PSS; Figure 5.4). In our experiments, the PSS formed at a distance of c. 200 μm from the asperities on the stationary side of the gouge holder (see location of dashed line in Figure 5.1c).

In all deformed samples, the bulk gouge layer was dominated by a striking foliation (Figure 5.4), defined primarily by an organized banding of heavily fractured dolomite- and calcite-rich domains (Figure 5.4). In common

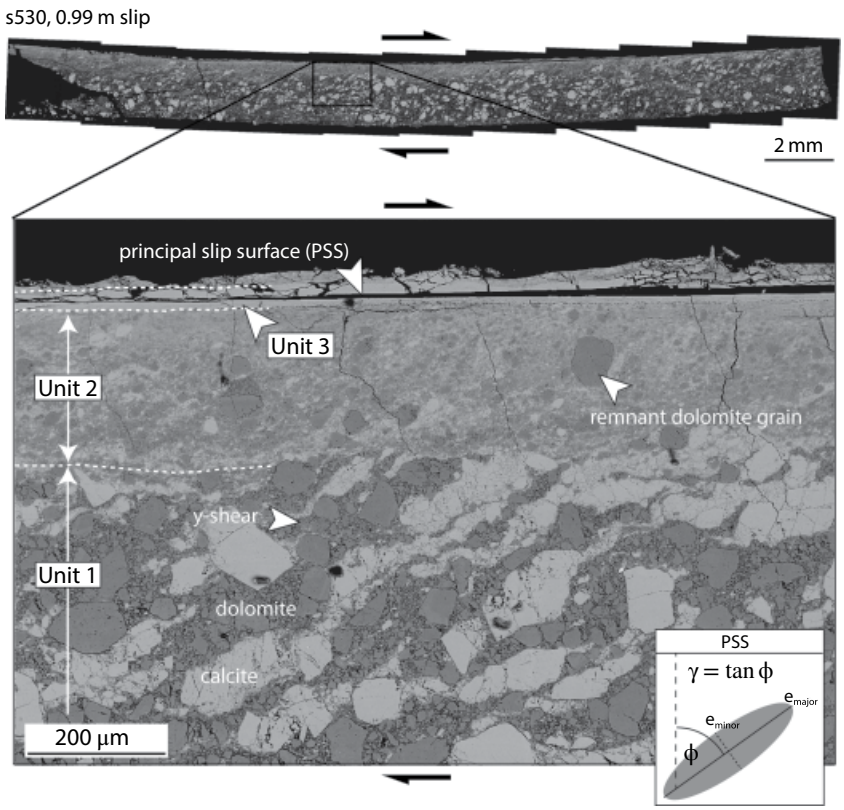

Figure 5.4 SEM images of gouge layer s530 showing a striking foliation and the definition of three microstructural units. The foliation occurs across a range of scales and is mainly defined by compositional banding of heavily fractured domains of calcite and dolomite. In sample s530, at distances >300 µm from the principal slip surface (labeled as unit 1), the foliated gouge retains relatively coarse grain sizes comparable to the starting materials. Closer to the principal slip surface (labeled unit 2), the foliated gouge has a much finer grain size with the exception of a few remnant dolomite grains. A layer c. 40 µm thick flanking the principal slip surface (labeled as unit 3) is very fine grained and has homogenous backscatter contrast. Inset shows the convention used to calculate and describe the orientations of the best-fit ellipses to each foliation domain (section 5.3.3.4).

with other high-velocity rotary shear experiments [e.g., *Kitajima et al.*, 2010), at least three distinct microstructural "units" were recognized on the basis of grain size variations, the degree of mixing between calcite and dolomite, and the general appearance of the foliation domains in optical and SEM images (Figure 5.4). The boundaries between the three microstructural units became sharper in samples with higher displacements (e.g., clear boundaries between units in s530 with 1 m displacement; Figure 5.4).

5.3.3.1.1. Microstructural Unit 1 Unit 1 contains relatively large (10–150 µm) intact grains of calcite and dolomite (similar in size to the starting materials, e.g., Figure 5.4). Most grains, however, are intensely fragmented and deformed into elongate domains of tightly packed and fine-grained (<10 µm) aggregates of calcite and dolomite that define the foliation (Figure 5.5a, b). Overall, the foliation has an anastomosing style characterized by domains of fractured calcite and dolomite with pinch-and-swell geometries (Figure 5.4). The foliation domains are generally inclined at approximately 45° to gouge layer boundaries (Figure 5.4; see quantitative analysis of foliations in section 5.3.3.4) but are sometimes deflected toward parallelism with gouge layer boundaries along Y-shears (Figure 5.4). Domains of fine-grained calcite and dolomite are up to 200 µm long and 100 µm wide, and derived in most cases from breakdown of single grains in the starting materials (Figure 5.5a). Large grains of calcite and dolomite have tails of fine-grained material (Figure 5.5c). The boundaries between calcite and dolomite domains are generally well defined and there is limited mixing between the two phases (Figure 5.5a). Interpenetration of small grains occurs across the boundaries between calcite and dolomite domains (Figure 5.5b). In areas where the calcite- or dolomite-rich domains become relatively thin, there is some mixing of small particles across phase boundaries (e.g., white arrows in Figure 5.5d point to small dolomite grains).

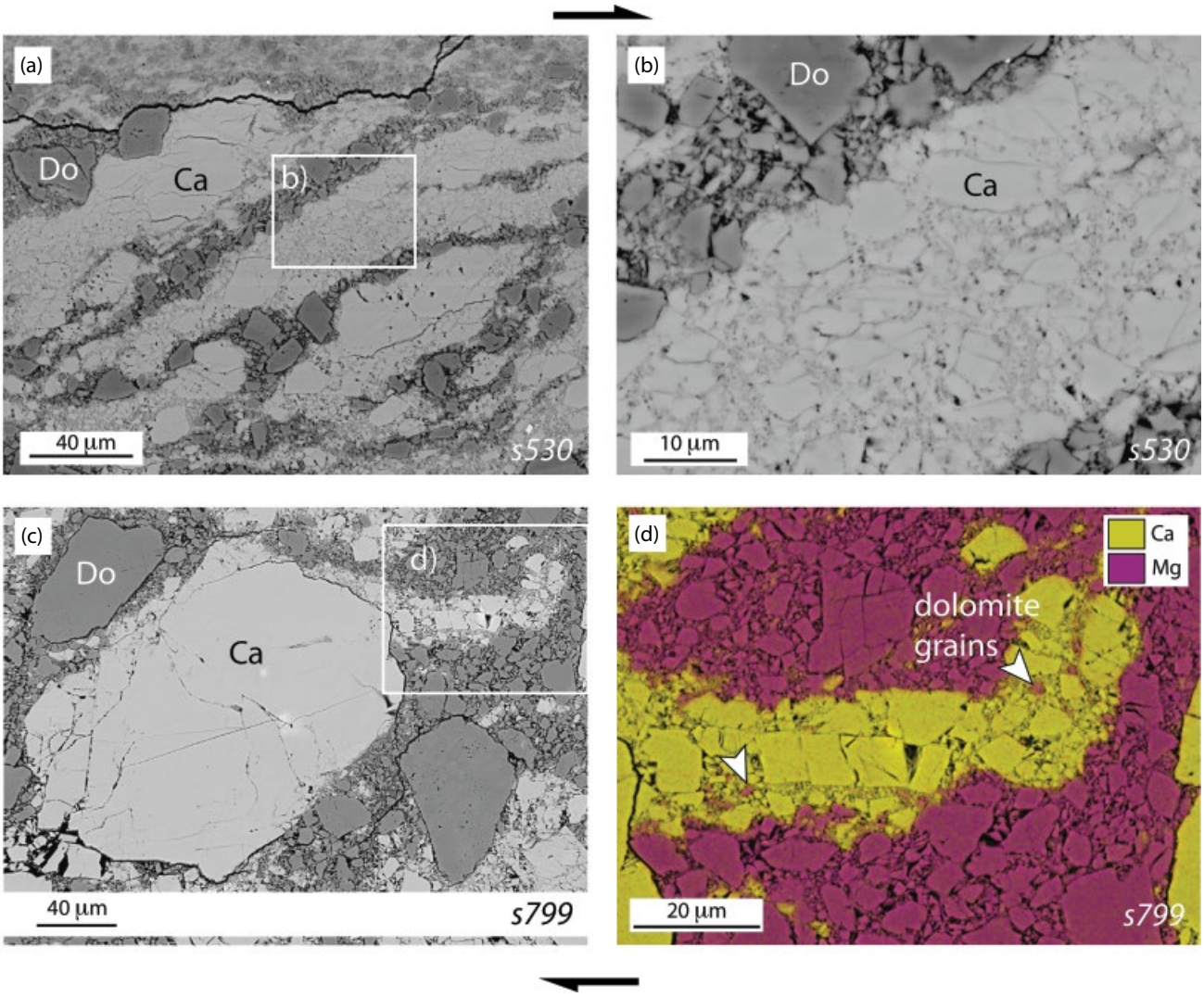

Figure 5.5 Microstructural unit 1. Images a–c are SEM images and d is an energy-dispersive X-ray spectroscopy (EDS) map. (a) Relatively large and elongate domains of heavily fractured calcite and dolomite define the foliation in microstructural unit 1. Domains are clearly distinguished and there is little mixing between the two phases. (b) Detail of boundary between calcite and dolomite foliation domains. The boundary is irregular due to interpenetration of small calcite and dolomite grains. (c) Large calcite grain with tail of heavily fractured calcite extending into dolomite-rich matrix. (d) Detail of calcite tail showing small particles of dolomite (white arrows) mixed with calcite.

5.3.3.1.2. Microstructural Unit 2 As in unit 1, the overall style of the foliation in unit 2 is anastomosing, and individual domains of dolomite and calcite have pinch-and-swell geometries (Figure 5.6a). Grain sizes in the matrix of unit 2 are generally <10 µm (Figure 5.6a), but remnant dolomite (and less frequent calcite) grains up to c. 50 µm in size are dispersed throughout (Figures 5.4, 5.6a). The remnant grains often have tails of fine-grained material (e.g., large calcite in Figure 5.6a) and resemble mantled porphyroclasts in mylonites. Foliation domains are shorter and thinner than in unit 1 (Figure 5.6a, b). In general, individual grains of calcite and dolomite <10 µm in size have sharp, angular to subangular shapes and are cut by intragranular fractures (Figure 5.6b). Although foliation domains are generally well defined in unit 2 (Figure 5.6a), there are areas where significant mixing has occurred between the two phases, resulting in a fine-grained matrix with a relatively homogenous distribution of calcite and dolomite (Figure 5.6b).

5.3.3.1.3. Microstructural Unit 3 Where present, unit 3 lies adjacent to the PSS and reaches a maximum thickness of c. 50 µm (Figures 5.4, 5.7a). Calcite in unit 3 is present in two forms: (1) as elongate grains up to 10 µm

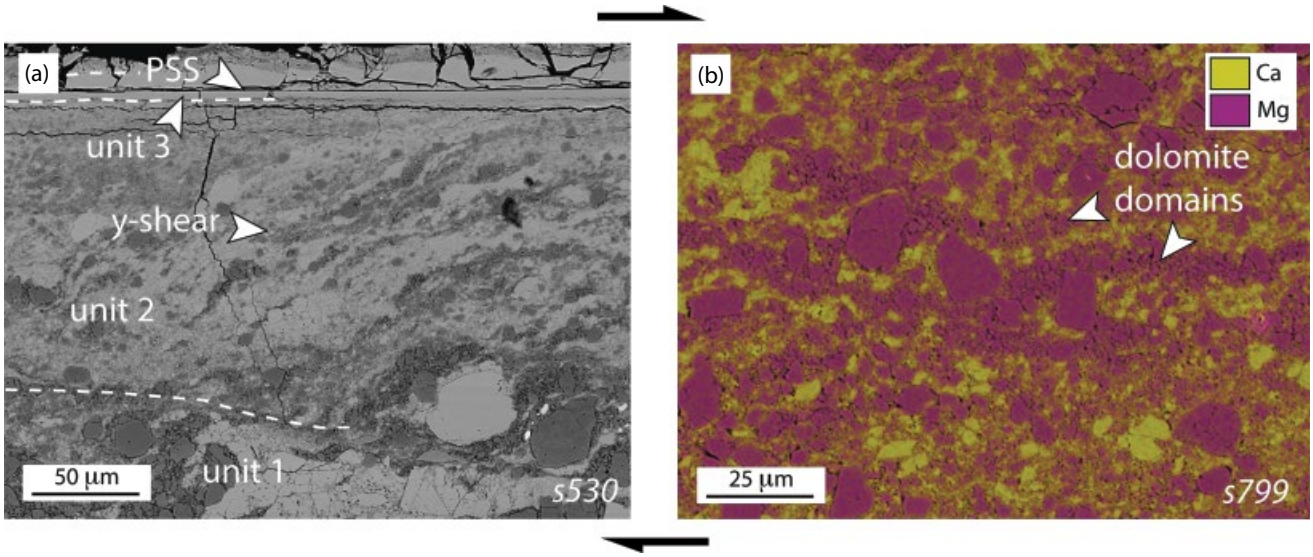

Figure 5.6 Microstructural unit 2. (a) SEM image showing relatively thin (compared to unit 1 in Figure 5.5) and elongate domains of calcite and dolomite. Grain size is smaller than unit 1 except for larger remnant grains. Image also shows the PSS flanked by microstructural unit 3. (b) EDS map showing two elongate domains of fine-grained dolomite (white arrows) subparallel to the PSS (top edge of image). Surrounding these domains, the matrix has a more homogenous distribution of calcite and dolomite.

long that are generally oriented obliquely to the PSS, forming aggregates with a grain shape preferred orientation (Figure 5.7a) and indistinct grain boundaries; and (2) as extremely fine grained (<1 µm) aggregates in which individual grains are not readily identifiable in SEM images (Figure 5.7b). These aggregates contain porous layers interbanded with domains that have little porosity and homogenous backscatter contrast (Figure 5.7b).

Dolomite grains up to c. 20 µm in size have sharp grain boundaries and are cut by intragranular microfractures (Figure 5.7a). Some dolomite grains also contain alignments and clusters of small holes that are interpreted as degassing-related porosity (Figure 5.7b), reported in more detail from calcite-dolomite gouge experiments by *Mitchell et al.* [2015]. Large dolomite grains embedded in unit 2 are typically truncated where they encounter one of the margins of unit 3 (Figure 5.7c). Similar truncated dolomite grains were reported by *Fondriest et al.* [2013] (in 100 wt% dolomite gouges) to form experimentally at high slip velocities ($V > 0.1$ m/s) and in association with the development of highly reflective (mirror-like) principal slip surfaces.

EDS analysis shows that the extremely fine grained (<1 µm) aggregates (e.g., Figure 5.7b) contain subtle layering defined by variations in the relative abundance of calcium and magnesium (Figure 5.7d). The grain size in such regions prohibited in-situ identification of mineral phases with the SEM. Powder X-ray diffraction performed on material derived from unit 3 (in the experiments with 0.05 m and 0.39 m displacement) revealed up to 28 wt% magnesian-calcite and trace amounts of periclase [*Griffiths*, 2014]. Neither of these phases was identified by X-ray diffraction in the starting materials or in the bulk gouge layers, suggesting that they are restricted to unit 3.

5.3.3.2. Evolution of Microstructural Units with Displacement

Mosaics of optical and SEM images were used to trace the distribution of microstructural units 1–3 in the five deformed samples used for quantitative microstructural analysis (Figures 5.8, 5.9). Unit 1 is dominant up to c. 0.2 m displacement (Figures 5.8, 5.9). In the sample with 0.03 m displacement, unit 1 is crosscut by R1 Riedel shears (using the terminology of *Logan et al.* [1979]) oriented approximately 15° to gouge layer boundaries (Figure 5.8a). With increasing displacement the Riedel shears disappeared and unit 1 was progressively replaced by units 2 and 3 (Figures 5.8, 5.9). The most significant change in the relative proportions of units 1 and 2 occurred during dynamic weakening (Figure 5.9). Unit 3 is first recognized as a thin lens along and adjacent to the PSS in the sample with 0.05 m displacement (Figure 5.8b). With increasing displacement, unit 3 becomes slightly thicker and more continuous along the PSS (Figure 5.8c–e), although only the sample with 0.39 m displacement contains a significant layer of unit 3 (Figure 5.9).

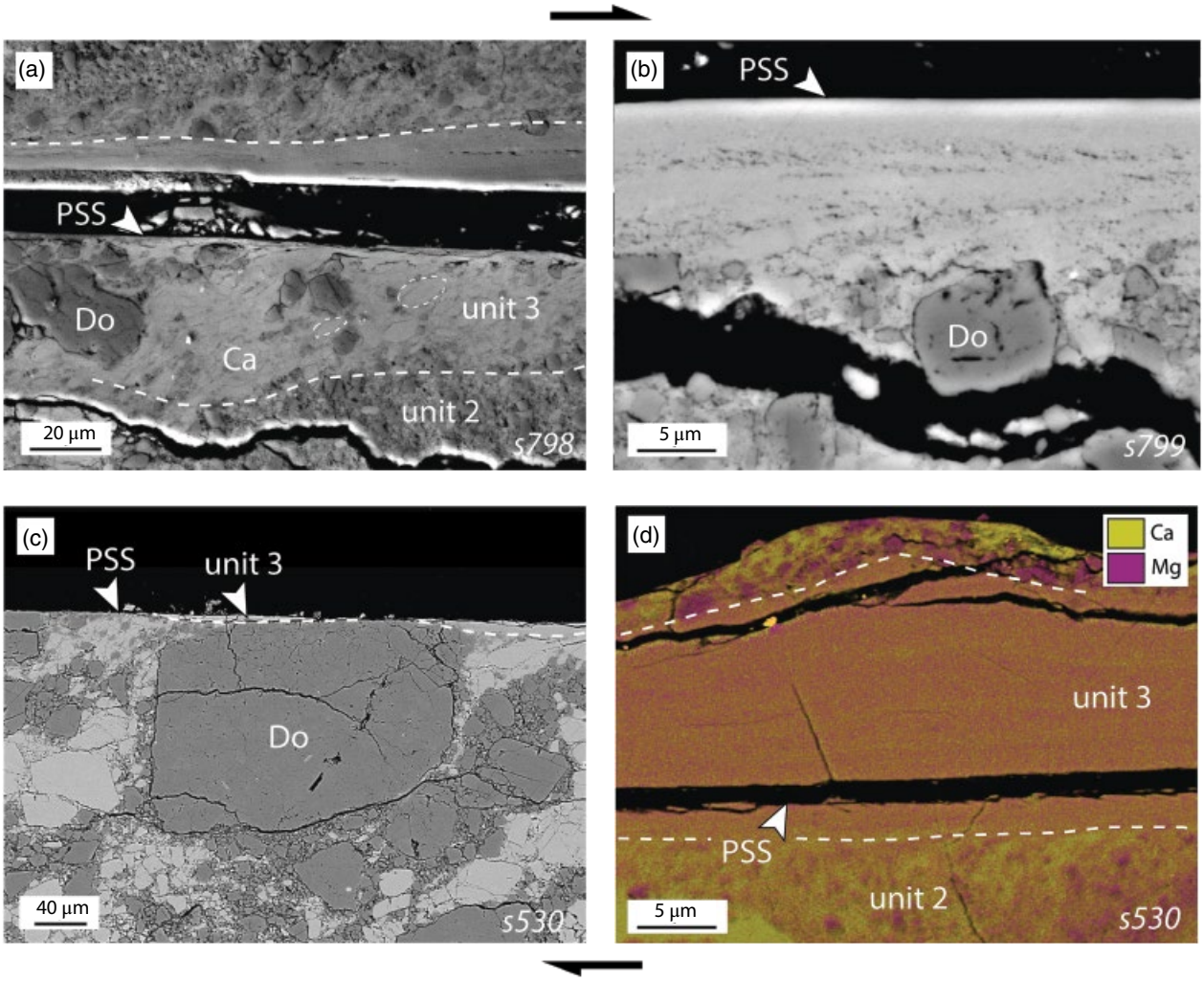

Figure 5.7 Microstructural unit 3. Images a–c are SEM images and d is an EDS map. (a) Unit 3 is up to 50 µm thick and flanks the PSS. In this example, aggregates of small (c. 5 µm) and elongate calcite grains (two examples surrounded by dashed lines) define a grain shape preferred orientation oblique to the PSS. Relatively large grains of dolomite are embedded in the calcite aggregates. (b) Very fine-grained calcite with indistinct grain boundaries forms aggregates with homogenous backscatter contrast adjacent to the PSS. Layering is defined by alignments of holes (pore space) parallel to the PSS. Dolomite grains adjacent to the aggregates contain pore space interpreted as degassing-related porosity. (c) Large dolomite grains embedded in microstructural unit 2 are sharply truncated at the margins of unit 3. (d) Diffuse banding in unit 3 defined by variations in the relative content of calcium and magnesium. *See electronic version for color representation*.

5.3.3.3. Fracturing Mechanisms in Microstructural Units 1 and 2

Intragranular microfractures in calcite and dolomite indicate that grain size reduction in units 1 and 2 occurred primarily by brittle fracturing (Figures 5.5, 5.6). Brittle fracturing is also interpreted as the dominant deformation mechanism in remnant dolomite grains in unit 3 (Figure 5.7a). Four main fracturing mechanisms were recognized:

1. *Impingement or "Hertzian" fracturing* (Figure 5.10a) occurred when two grains of the same phase (calcite or dolomite) and roughly the same size were brought into contact. Such fractures likely formed by tensile failure of grains when load was supported across grain bridges (or "force chains") [e.g., *Mair and Hazzard*, 2007; *Sammis and Ben-Zion*, 2008]. This mechanism was particularly prevalent in dolomite grains (Figure 5.10a) but was also observed in calcite. Typically, the fractures associated with this mechanism radiate from a contact region between the two colliding grains, producing elongate grain fragments (or "beams"). The example in Figure 5.10a shows trails of calcite that originate at the

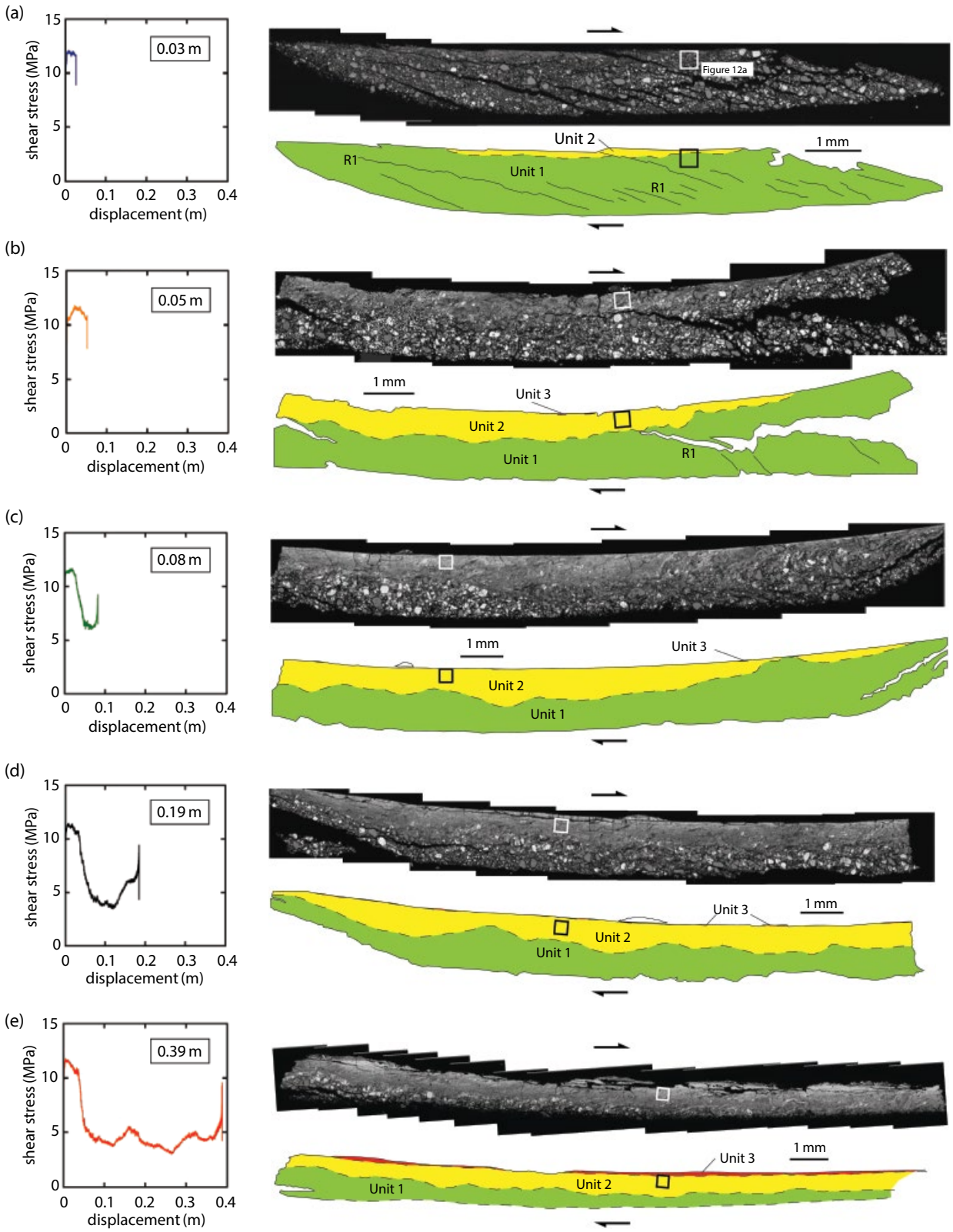

Figure 5.8 Evolution of microstructural units 1–3 with increasing displacement. Each Figure part (a–e) shows a plot of shear stress vs. displacement (same data as shown in Figure 5.3a), and a SEM mosaic and corresponding line tracing of the distribution of units 1–3. Boxes on the SEM mosaics and line tracings show the locations of analysis areas in Figure 5.12a. (a) 0.03 m displacement, (b) 0.05 m displacement, (c) 0.08 m displacement, (d) 0.19 m displacement, (e) 0.39 m displacement.

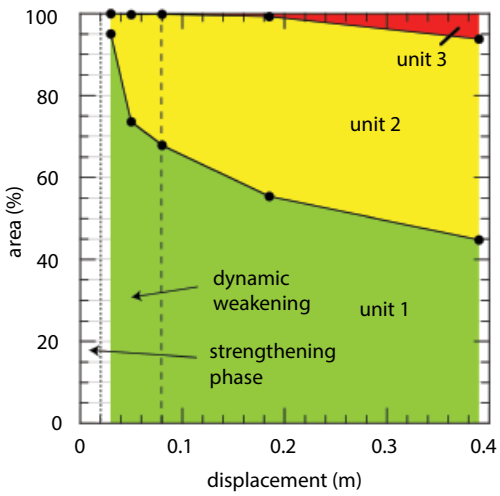

Figure 5.9 Plot showing the area of sample occupied by microstructural units 1–3 vs. displacement. With increasing displacement, microstructural unit 2 becomes proportionally more important than unit 1. Unit 3 is recognizable after 0.05 m of slip (0.2% of sample area) but increases significantly only after 0.2 m of slip.

contact region between two large dolomite grains. This is interpreted as a calcite grain that was pulverized and expelled outward as the two dolomite grains moved closer together during shearing.

2. *Spalling and chipping* (Figure 5.10b) of angular fragments occurred along the outer margins of calcite and dolomite grains [*Billi*, 2009]. This produced grains with a central, relatively intact fragment (white dashed line, Figure 5.10b) and an outer mantle of finer-grained material defining an overall subrounded grain shape (black dashed line, Figure 5.10b).

3. *Breakdown of polycrystalline dolomite particles* (Figure 5.10c) by fracturing along grain boundaries produced aggregates of fine-grained gouge. The example in the center of Figure 5.10c is interpreted as a polycrystalline dolomite particle, most probably of the granular type described in section 5.3.1, that broke down into its constituent single grains during shearing.

4. *Fracturing of cleavage planes* (Figure 5.10d) in calcite (and more rarely in dolomite) occurred systematically in orientations at c. 45°–55° to gouge layer boundaries (angle measured clockwise in Figure 5.10d). Similar fracture orientations are observed also for the "Hertzian" fracturing mechanism (Figure 5.10a).

5.3.3.4. Foliation Geometry and Shear Strain in Deformed Gouge Layers

In each deformed sample, SEM images (e.g., Figure 5.4) and EDS maps were used to outline individual domains of calcite and dolomite that collectively define the foliation (Figure 5.4). Outlines of calcite- and dolomite-rich domains were imported into Image SXM software and used to calculate the best-fit ellipse for each domain (Figure 5.4, inset). The orientation of the major axis of the best-fit ellipse is represented by the angle, ϕ, which was used as a proxy for shear strain, $\gamma = \tan \phi$ (Figure 5.4, inset). This analysis was performed for many individual calcite- and dolomite-rich domains in microstructural units 1 and 2 to obtain measurements of the angles between each foliation domain and the PSS, and therefore proxy shear strain, across most of the thickness of each gouge layer (Figure 5.4). The assumption that the orientation of foliation domains is a reasonable proxy for shear strain is made on the basis that (i) domains of calcite and dolomite used in the analysis were derived from breakdown of single large grains in the gouge starting material, (ii) most grains in the starting material are roughly equidimensional and the starting material shows homogenous mixing between the two phases, and (iii) in terms of the values of strain and the overall strain distribution (Figure 5.11), our analysis gives comparable results to other high-velocity gouge experiments in which tabular strain markers were used to track the shear strain distribution [*Rempe et al.*, 2014; *Smith et al.*, 2015].

In the sample with 0.03 m displacement, foliation domains are inclined (angle ϕ) at approximately 45°–50° to gouge layer boundaries, corresponding to a shear strain of $\gamma \sim 1.5$ across the measured thickness of the gouge layer (Figure 5.11a). In this sample, data were not collected from >600 μm from the stationary side of the gouge layer, but the grain size preserved in that area is similar to the starting materials, and thus it is unlikely that γ was higher than c. 1.5. Due to fine grain size, data were also not collected from within c. 50 μm of the stationary side of the gouge layer. However, the bulk shear strain in this gouge layer is 15 (Table 5.1), calculated as the total displacement (0.03 m) divided by the gouge layer thickness (2 mm). This indicates that most strain (>90%) in this sample is focused into a layer <50 μm thick along the stationary side (Figure 5.11a). This layer corresponds to the incipient development of microstructural unit 2 (Figure 5.8a), which therefore represents a relatively high-strain "shear band" compared to microstructural unit 1.

After 0.05 m displacement, foliation domains closer than c. 200 μm to the newly-formed PSS rotate progressively toward parallelism with the PSS, defining a zone with $\gamma > 1.5$ (Figure 5.11b). At distances greater than c. 200 μm from the PSS, foliation domains remain at c. 45°–50° to gouge layer boundaries (Figure 5.11b). The zone with $\gamma > 1.5$ then becomes progressively wider (i.e., migrates away from the PSS) with increasing displacement (Figures 5.11b–e). This zone ($\gamma > 1.5$) can be correlated with microstructural unit 2 (Figure 5.11), which becomes wider (Figure 5.8) and proportionally dominant (Figure 5.9) with increasing displacement. It is

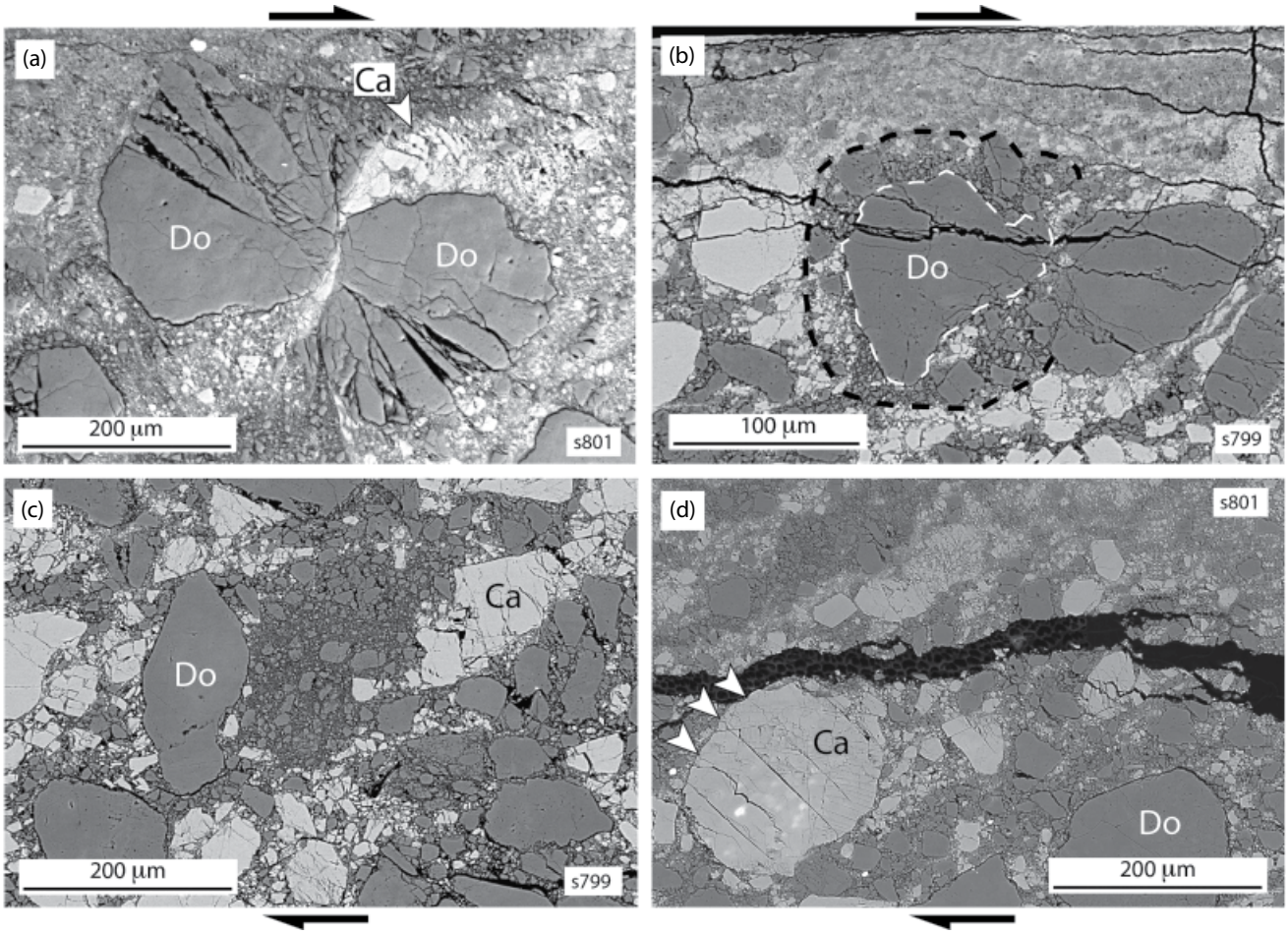

Figure 5.10 SEM images illustrating the four main fracturing mechanisms identified in microstructural units 1 and 2. (a) Hertzian or impingement fracturing between two large dolomite grains in sample s801 (0.05 m slip). As they were brought into contact, the two large dolomite grains are interpreted to have "squeezed out" an intervening calcite grain that is preserved as tails of fine-grained material emanating from the contact region. (b) Spalling of fine-grained material from the outer margin of a large dolomite grain in sample s799 (0.39 m slip). White dashed lines surround central grain, black dashed lines surround outer mantle of fragmented material. (c) The aggregate of fine-grained dolomite in the center of the image is interpreted to derive from breakdown of a polycrystalline dolomite particle similar to that shown on the left of Figure 5.2b. Sample s799 (0.39 m slip). (d) Planar fractures (white arrows) in sample s801 (0.05 m slip) form along cleavage planes in calcite that are oriented at c. 45°–55° to gouge layer boundaries (angle measured clockwise).

evident that at higher displacements in unit 2, most notably at 0.19 m (Figure 5.11d) and 0.39 m (Figure 5.11e), there is much more scatter in the measured strain values, reflecting progressive mixing and disaggregation of grains comprising the foliation domains.

We stress that in each of these samples (Figure 5.11), the bulk γ values (Table 5.1) dictate that most displacement (strain) in the experiments must be accommodated within a high-strain layer that is not represented in our measurements of foliation angle/shear strain from microstructural units 1 and 2 (Figure 5.11). At relatively small displacements, the high-strain layer corresponds to the incipient microstructural unit 2 (Figure 5.11a), whereas at larger displacements the high-strain layer corresponds to microstructural unit 3 and a discrete PSS embedded within unit 3 (Figures 5.11b–e).

5.3.3.5. Grain Size Analysis

The size of calcite and dolomite grains was quantitatively evaluated from an area of 300 μm^2 in the starting materials and each deformed gouge sample (Figure 5.12a). The analysis areas for the deformed samples are shown in Figure 5.8. In the deformed samples, the analysis areas all have their upper edges along and parallel to the PSS (Figure 5.8). This was done to ensure that the analysis areas covered the regions of gouge that show a clear

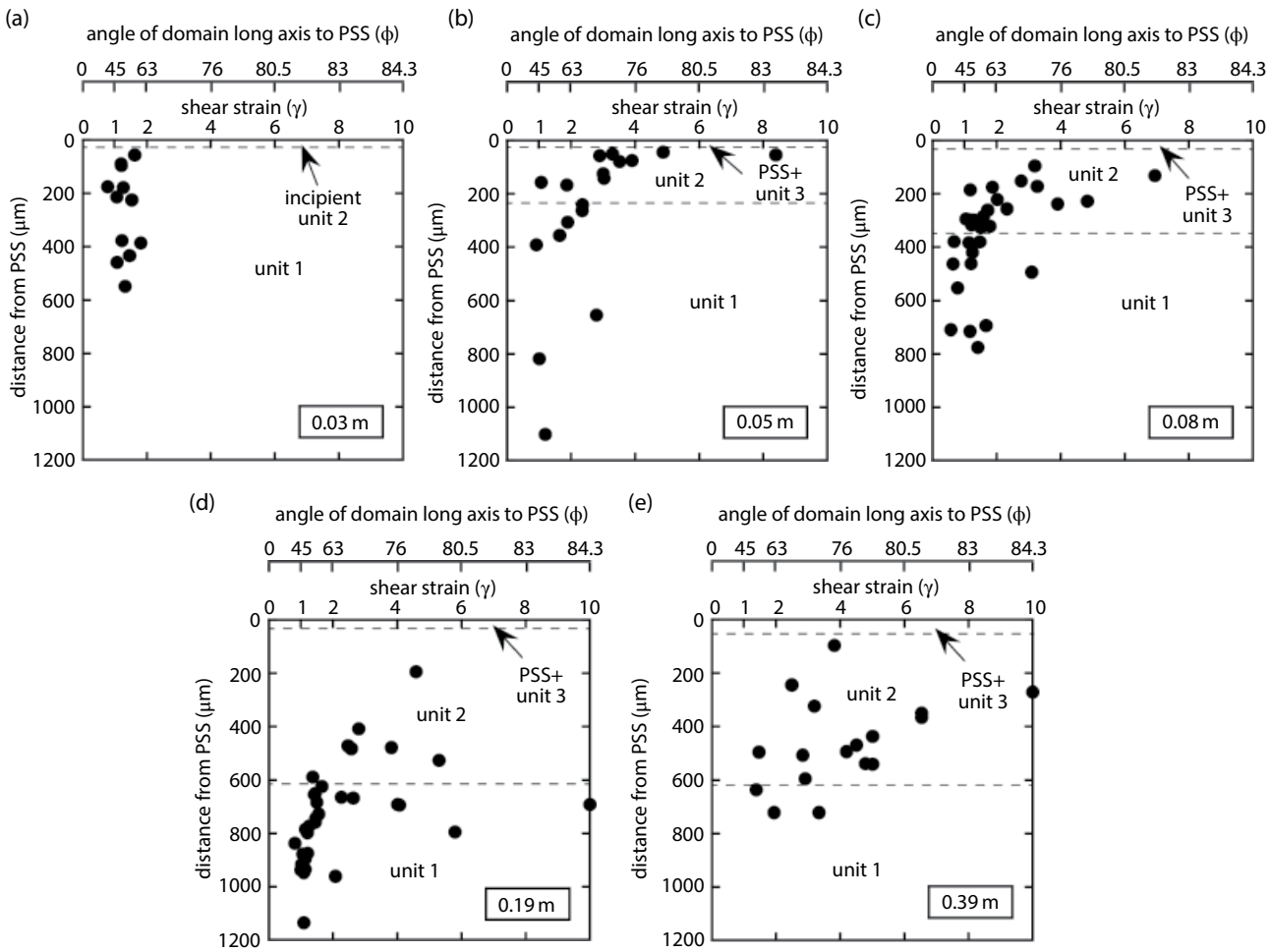

Figure 5.11 Results of shear strain analysis. Plots show shear strain vs. distance from the PSS in samples with increasing displacement. Each data point is a measurement of shear strain calculated from the angle of one foliation domain (convention in Figure 5.4 inset). Dashed horizontal lines show the boundaries between microstructural units 1, 2, and 3. (a) 0.03 m displacement, (b) 0.05 m, (c) 0.08 m, (d) 0.19 m, (e) 0.39 m.

evolution of fabric and strain with displacement (i.e., the inception and evolution of microstructural unit 2; Figure 5.11).

An area of 300 μm^2 was selected for each sample, and images (Figure 5.12a) were prepared showing grains of calcite and dolomite (and matrix) using the methods detailed in [*Griffiths*, 2014]. The minimum pixel dimension of grains that could be reliably identified and used for grain size analysis was set as 25 pixels^2, corresponding to a grain diameter of approximately 1.2 μm. Grain size was measured in Image SXM and calculated as the diameter of an equivalent circle, $d_{equ} = 2\sqrt{A/\pi}$, where A is the measured area of the grain.

Results show that both the mean and maximum grain size in the analysis areas decreases significantly during the first 0.08 m of displacement, coinciding with the strengthening and dynamic weakening phases observed in mechanical data (Figures 5.12a, b). Mean grain size decreases to a greater extent in calcite than dolomite (Figure 5.12a). By the time that dynamic weakening has ended, grain size in the analysis areas has stabilized (Figures 5.12b, c). However, the mean grain size of calcite (and to a lesser extent dolomite) slightly increases again in the sample with 0.39 m displacement (Figure 5.12a).

5.3.3.6. Clast Size Distribution Analysis

Two-dimensional clast size distributions (CSDs) were determined for calcite and dolomite in the starting materials and five deformed samples using the grain size data described in the preceding section (i.e., images shown in Figure 5.12a). For each sample, the cumulative number of clasts, N, larger than a given diameter, d_{equ}, was plotted in $\log(N) - \log(d_{equ})$ diagrams (Figure 5.13). CSD curves following a good linear fit over a restricted dimensional range were described by a power-law relationship $N \sim d_{equ}^{-D}$ ($\log(N) \sim -D\log(d)$), where D is the fractal dimension.

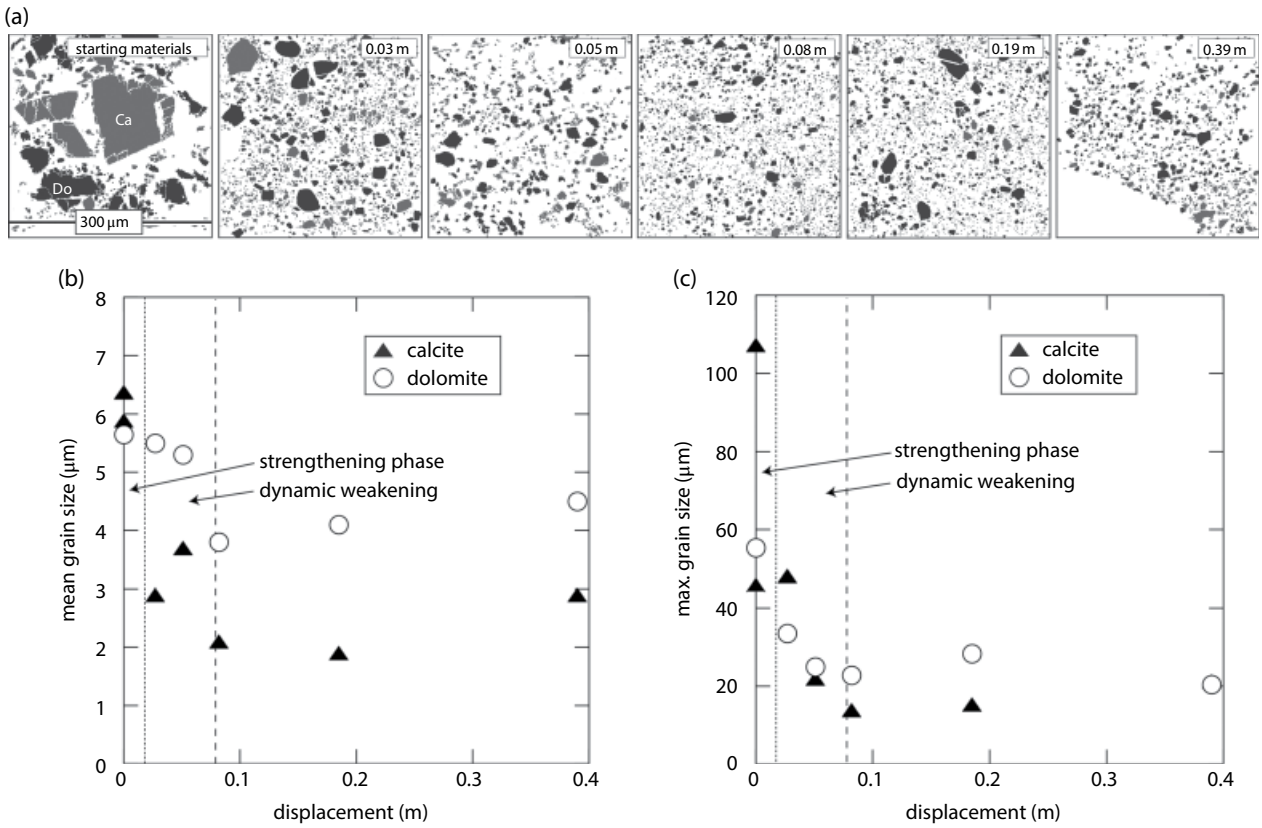

Figure 5.12 Grain size analysis. (a) Grayscale images used to calculate grain size statistics in the starting materials and five deformed gouge samples. The location of each image is shown (for the deformed samples) in Figure 5.8. Images are 300 µm × 300 µm. Numbers at top of images are displacement values. (b) Mean grain size vs. displacement. For calcite in the starting materials (i.e., 0 m displacement) two values are given: the higher value includes the largest grain shown in Figure 5.12a, the lower value excludes the largest grain shown in Figure 5.12a. (c) Maximum grain size vs. displacement.

The "strength" of the power-law relationship over the analyzed fractal range is shown by the value of R^2 (correlation coefficient), which is between 0.98 and 0.99 for the best-fit lines in the log-log distributions in all samples. We note that both the minimum and maximum grain sizes in the log-log distributions (Figure 5.13) are artificially constrained by, respectively, the lower cutoff in grain size that we imposed during image analysis and the maximum grain size used in the starting materials. As commonly observed in datasets of this type, there is a rollover effect at small grain sizes due to small particles being relatively difficult to detect and measure at a given scale of observation [*Blenkinsop*, 1991; *Fagereng*, 2011]. In our datasets, this rollover is observed at a characteristic grain size of <2 µm for calcite and c. 3–4 µm for dolomite (start of rollover indicated by arrows in Figure 5.13). The rollover parts of the CSD curves were left out when fitting a straight line to the log-log plots. Our results also cover a limited dimensional range (up to two orders of magnitude). For these reasons, we use D only to quantify relative differences between our experimental samples and to reveal aspects of the grain size distributions that are not apparent by simply plotting mean and maximum grain sizes (Figure 5.12).

The CSDs of calcite and dolomite in the starting materials (Figure 5.13a) cover a clast size range of 1.5–60 µm and are characterized by two segments with distinctly different D values: a shallower segment at relatively small grain sizes (<8 µm) with D values of 0.9 (calcite) to 1 (dolomite), and a steeper segment at larger grain sizes (>8 µm) with D values of 1.75 (calcite) to 1.8 (dolomite). The D values for deformed samples are adequately fit by power-law distributions over most of the analyzed range of grain sizes. The D values of both calcite and dolomite increase substantially in the first 0.08 m of slip, from $D < 1.8$ in the starting materials to $D \approx 3$ by the end of dynamic weakening (Figure 5.14). With increasing displacement above 0.08 m, the D values remain roughly constant (Figure 5.14).

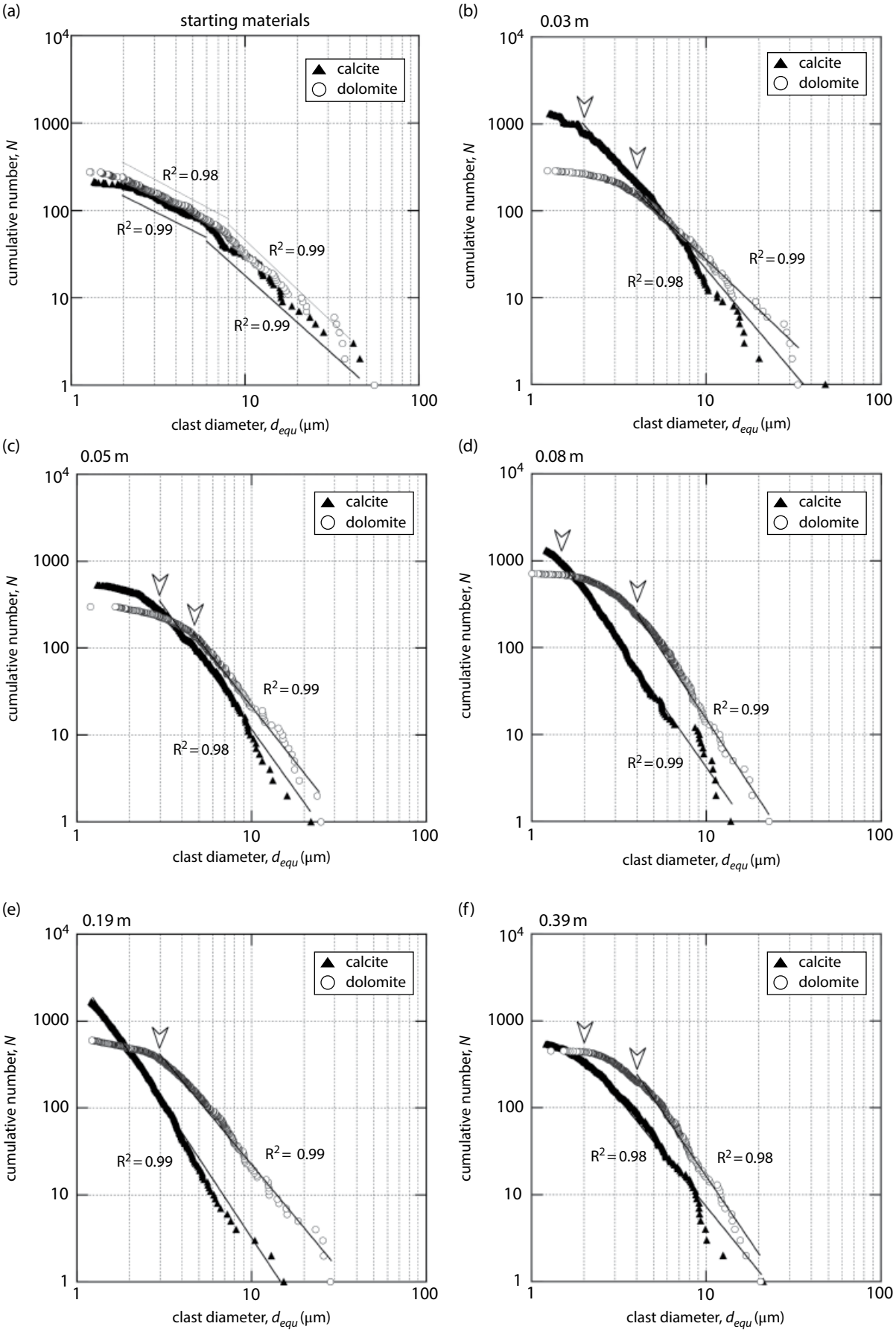

Figure 5.13 Plots of log grain size (d_{equ}) vs. cumulative number (N). See text for details of method. Arrows indicate the smallest grain size used to calculate the 2-dimensional "fractal" dimension, D, from linear best-fit lines. (a) Starting materials. (b–f) Samples with increasing displacements between 0.03 m and 0.39 m.

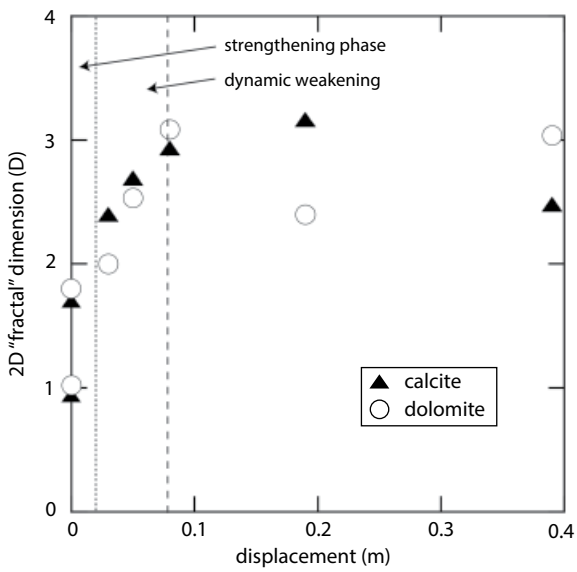

Figure 5.14 Plot showing the evolution of the 2-dimensional "fractal" dimension, *D*, with increasing displacement. For the starting materials, two *D* values are given corresponding to the shallower and steeper segments of the CSD curves observed on the log-log plot in Figure 5.13a.

5.4. DISCUSSION

5.4.1. Fabric Development and Grain Size Reduction at High Slip Velocities

Our experiments indicate that at high slip velocities ($V > 0.01\,\mathrm{m\,s^{-1}}$) and for displacements representative of earthquakes of approximately M_w 3–7, well-defined foliations can form in calcite-dolomite gouges from an initial mixed distribution of phases. Microstructural data document a progressive evolution of fabric and grain size that strongly correlates with gouge mechanical behavior. The most significant changes in microstructure, fabric geometry, and grain size in our experiments occurred before and during dynamic weakening. Once shear stress reached "steady state," after approximately 0.08 m in these experiments, fabric and grain size in the bulk gouge layers essentially stabilized and did not experience further changes. In the following paragraphs, we build on previous work [e.g., *Kitajima et al.*, 2010; *Yao et al.*, 2013; *Bullock et al.*, 2015; *De Paola et al.*, 2015; *Smith et al.*, 2015] and interpret our results in the context of shear localization and the development of a PSS in the gouge layers (Figure 5.15).

During the initial gouge strengthening phase, strain was homogenously distributed ($\gamma \sim 1.5$) across the bulk of the gouge layer and R1 Riedel shears were active (Figure 5.15a). A striking foliation developed (to form our microstructural unit 1) that we interpret to result from a combination of processes: grain size reduction occurred primarily by breakdown of polycrystalline grains and fracturing of large grains in the starting materials. Where discrete intragranular fractures occur, they show a strong preferred orientation subparallel to the instantaneous shortening direction (σ1) during simple shear (Figure 5.15a). Such fractures likely form by tensile failure of grains because load is supported across grain bridges (or "force chains") that develop in the gouge layers subparallel to the σ1 direction [e.g., *Mair and Hazzard*, 2007; *Sammis and Ben-Zion*, 2008]. Microstructures suggest that many grains (but particularly calcite grains) fractured when they rotated into an orientation such that a set of cleavage planes was subparallel to σ1 (Figure 5.15a). Fracturing throughout the gouge layer during initially distributed shearing produced fine-grained aggregates that were soft and readily deformable. The orientation of foliation domains at c. 45°–50° to gouge layer boundaries suggests that aggregates were compressed subparallel to σ1 and elongated subperpendicular to σ1 (Figure 5.15a). Together with the effects of distributed strain, this formed a foliation defined by elongate domains of crushed calcite and dolomite (Figure 5.15a). The overall low strain in microstructural unit 1 ($\gamma \sim 1.5$) meant that there was minimal mixing between calcite and dolomite. By the end of the initial strengthening phase, strain had started to localize close to one margin of the gouge layer (Figure 5.15a; incipient microstructural unit 2).

During the dynamic weakening phase, lenses of microstructural unit 3 and a through-going PSS were established, accommodating most subsequent displacement at high strain rates (Figure 5.15b). Despite this progressive localization process during dynamic weakening, the gouge adjacent to the PSS also continued to deform (Figure 5.15b). This is indicated in our experiments by widening of microstructural unit 2 and rapid grain size reduction in unit 2 observed during dynamic weakening (Figure 5.15b). Grain size reduction caused an increase in the *D* values of the grain size distributions (Figure 5.14). However, the evolution of mean grain sizes (Figure 5.12b) and the common occurrence of relatively large remnant dolomite grains in units 2 and 3 indicate that dolomite was more resistant overall to grain size reduction.

The formation and evolution of microstructural unit 3 during dynamic weakening is interpreted to result from recrystallization and decomposition of fine-grained calcite and dolomite along and adjacent to the PSS (Figure 5.15c), driven by the frictional heat produced as a consequence of localized slip at high strain rates. Indistinct calcite grain boundaries (even at high magnifications in the SEM) and the grain-shape preferred orientation observed in some calcite aggregates in unit 3 (Figure 5.7a) suggest calcite recrystallization and grain welding. This is consistent with the detection in unit 3 of magnesian-calcite and periclase, probably formed by decomposition of dolomite at temperatures exceeding c. 550 °C

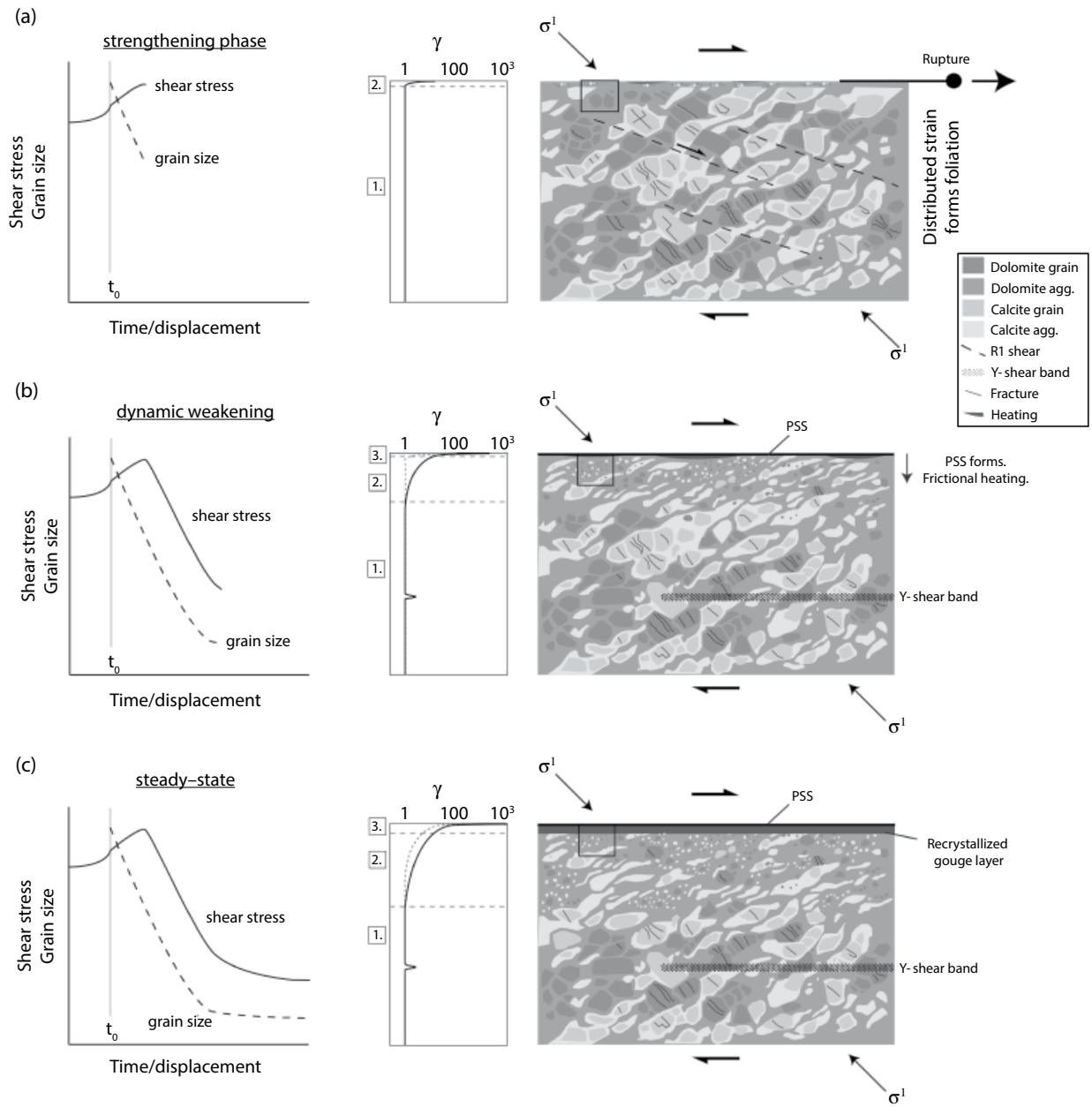

Figure 5.15 Schematic synthesis of mechanical behavior and fabric evolution observed in mixed calcite-dolomite gouge experiments. Numbers in boxes refer to the microstructural units described in this chapter. (a) The initial stages of coseismic shearing are distributed across the gouge layer. R1 Riedel shears are active. Foliation develops by a combination of pervasive grain fracturing and rotation of individual foliation domains at relatively low strains. This accompanies strengthening observed in the mechanical data. By the end of the strengthening phase, strain has started to localize in a narrow band (microstructural unit 2) that will ultimately develop into a discrete PSS surrounded by microstructural unit 3. (b) Dynamic weakening accompanies progressive formation of a discrete PSS associated with lenses of unit 3. The PSS (and possibly unit 3) accommodates most subsequent displacement, but the gouge adjacent to the PSS also continues to deform, resulting in widening of microstructural unit 2. Y-shears form in the bulk gouge. (c) The PSS (and possibly unit 3) continues to accommodate most displacement once "steady-state" shear stress is attained. Frictional heating along the PSS causes decomposition of the carbonates and forms a semicontinuous layer of recrystallized gouge (microstructural unit 3) that becomes slightly thicker with increasing displacement. No significant changes to grain size or gouge fabric take place in units 1 and 2 once steady state is achieved.

[*Samtani et al.*, 2002; *De Paola et al.*, 2011; *Fondriest et al.*, 2013]. Our interpretation of unit 3 is also based on previous high-velocity experimental work documenting the formation of recrystallized "mylonitic" layers due to frictional heating along a discrete slip surface [*Kim et al.*, 2010; *Brantut et al.*, 2011; *Smith et al.*, 2013; *Ree et al.*, 2014; *De Paola et al.*, 2015; *Green et al.*, 2015]. It is noteworthy that the grain size of recrystallized calcite in microstructural unit 3 (<1 μm in the aggregates; Figure 5.7b) is much smaller than in experiments performed with pure (100 wt%) calcite gouge under similar conditions [*Smith et al.*, 2013; 1–10 μm with ribbon grains up to 50 μm]. We suggest that this is because dolomite inhibits recrystallization and postexperiment grain growth in calcite by effectively "pinning" calcite grain boundaries [*Herwegh and Kunze*, 2002; *Delle Piane et al.*, 2009].

After "steady-state" shear stress was attained in the experiments (Figure 5.15c), the PSS (and possibly microstructural unit 3) continued to accommodate most ongoing displacement at high strain rates, although unit 2 widened slightly, indicating that the bulk gouge also continues to deform (Figure 5.15c). Microstructural unit 3 increased in thickness to form a semicontinuous layer of recrystallized gouge as a result of continued frictional heating (and decomposition) along the PSS [*Smith et al.*, 2013].

We emphasize that although the strain rate along the PSS, and potentially within microstructural unit 3, must have been extremely high, the strain rates in the adjacent layers (microstructural units 1 and 2) throughout the experiments were much lower. Strain accommodated in microstructural unit 2 only increased from c. 1.5 to c. 8–10 during dynamic weakening (Figure 5.11). Nevertheless, this modest increase in strain was enough to cause substantial mixing of calcite and dolomite grains, as well as thinning and disaggregation of the foliation domains (Figure 5.15b). In microstructural unit 1, deformation essentially ceased once peak stress was reached and strain had localized to units 2–3 and the PSS (Figure 5.15b, c). Summarizing, progressive fabric, and grain size evolution in the bulk gouge layers occurred by cataclastic "flow" at relatively low strains and strain rates, in parallel with deformation occurring at high strain rates along the bounding PSS.

5.4.2. A Coseismic Origin for Some Foliated Gouges and Cataclasites?

In the cores of natural faults exhumed from depths of c. 5–15 km, foliations present in gouge and cataclasite are commonly defined by interconnected networks and overgrowths of aligned phyllosilicate phases [e.g., *Imber et al.*, 1997; *Manatschal*, 1999; *Stewart et al.*, 2000; *White*, 2001; *Wintsch and Yi*, 2002; *Gueydan et al.*, 2003; *Collettini and Holdsworth*, 2004; *Jefferies et al.*, 2006; *Collettini et al.*, 2009; *Wallis et al.*, 2013]. In this type of foliated gouge and cataclasite, there is abundant microstructural and geochemical evidence for the operation of frictional sliding accompanied by fluid-assisted deformation processes and dissolution-precipitation reactions. In such cases, a convincing argument has been made that the phyllosilicate-rich foliations were generated during aseismic fault creep, perhaps at low stresses leading to long-term fault zone weakening [*Rutter et al.*, 2001; *Holdsworth*, 2004; *Moore and Rymer*, 2007]. Experiments on clay-bearing gouge layers at low slip velocities indicate that mechanical rotation of clay particles can also form well-defined foliations [*Rutter et al.*, 1986; *Logan et al.*, 1992; *Haines et al.*, 2013]. *Bos et al.* [2000] and *Niemeijer and Spiers* [2006] showed that foliations defined by aligned and interconnected phyllosilicate seams developed in brine-saturated gouge experiments at low strain rates by granular flow accompanied by efficient dissolution-precipitation. In the same experiments, an increase in strain rate led to disruption of the foliation and formation of a random-fabric gouge [*Niemeijer and Spiers*, 2006].

In many other cases, foliations in natural gouge and cataclasite reflect the combined influences of compositional layering, grain size variations, preferred alignment of clasts and fractures, or an organized arrangement of shear surfaces [e.g., *Chester and Logan*, 1987; *Chester and Chester*, 1998; *Fabbri et al.*, 2000; *Lin*, 2001; *White*, 2001; *Cowan et al.*, 2003]. These types of foliated gouge and cataclasite are particularly common in brittle fault zones exhumed from depths of less than about 10 km, where grain size reduction by cataclasis is expected to become a dominant deformation mechanism [*Sibson*, 1977]. Although an "aseismic" interpretation is often adopted for the origin of such foliated cataclasites, our experimental gouges deformed at seismic slip velocities ($V < 1.13\,\mathrm{m\,s^{-1}}$) contain striking foliations defined primarily by compositional layering and grain size variations. This suggests that some natural examples of foliated gouge and cataclasite with similar microstructure may be better interpreted as the product of distributed brittle "flow" during coseismic slip, particularly if the foliations are found in conjunction with a bounding slip surface.

In our gouge experiments, the most striking foliations were established in the gouge layers at relatively low strain ($\gamma < 1.5$), as deformation was progressively localized before and during the dynamic weakening process. In natural fault zones, few constraints are currently available on the initial thickness (or grain size distribution) of the coseismic shear zone that starts to deform after passage of the rupture front [*Beeler et al.*, 2008]. Based on field and borehole observations in active and exhumed faults, it is not unreasonable to think that the initial stages of coseismic shearing in large fault zones may be accommodated in gouge or breccia horizons exceeding tens of centimeters or more in thickness [*Sibson*, 2003, *Sagy and Brodsky*, 2009]. If this is true, initially distributed shearing

in such horizons may be sufficient to form "coseismic foliations" that occupy relatively thick fault rock layers, even if strain quickly localizes to a narrow band or slip surface.

5.5. CONCLUSIONS

High-velocity ($V < 1.13$ m/s) shear experiments on mixed calcite-dolomite gouges were performed to investigate fabric and grain size evolution and to explore the possibility that some natural foliated fault rocks may have a coseismic origin. Results indicate that for displacements representative of earthquakes of approximately M_w 3–7, foliations can develop quickly from an initial mixed assemblage of calcite and dolomite grains. The most significant changes in gouge microstructure, foliation geometry, and grain size take place before and during dynamic weakening, as initially distributed strain becomes localized to a discrete slip surface. Formation of the slip surface is complete by the end of dynamic weakening, after which foliation and grain size in the bulk gouge layer stabilize and do not experience significant further changes. Although an "aseismic" interpretation is often adopted for the origin of foliated gouge and cataclasite in brittle fault zones, our experiments suggest that foliations defined by compositional banding, grain size variations, and preferred particle or fracture alignments could form by distributed brittle flow as strain localizes during coseismic shearing.

ACKNOWLEDGEMENTS

This work was supported by the Marsden Fund Council (project UOO1417 to Smith), administered by the Royal Society of New Zealand, ERC StG no. 205175 USEMS (to Di Toro) and ERC CoG no. 614705 NOFEAR (to Di Toro). Marco Brenna and Kat Lilly provided assistance with the SEM in the Otago Centre for Electron Microscopy (OCEM) at the University of Otago. Brent Pooley prepared excellent thin sections. Fabio de Felice and Elena Spagnuolo provided assistance with experiments at the INGV, Rome. Marianne Negrini helped with preparation of figures. Christie Rowe and Rachel Bullock providing constructive reviews that helped to clarify many aspects of the paper.

REFERENCES

Beeler, N. M., T. E. Tullis, and D. L. Goldsby (2008), Constitutive relationships and physical basis of fault strength due to flash heating, *Journal of Geophysical Research: Solid Earth*, *113*(B1).

Billi, A. (2009), Microtectonics of low-P low-T carbonate fault rocks, *Journal of Structural Geology 32*, 1392–1402.

Blenkinsop, T. G. (1991), Cataclasis and processes of particle-size reduction, *Pure and Applied Geophysics*, *136*(1), 59–86.

Bos, B., C. J. Peach, and C. J. Spiers (2000), Frictional-viscous flow of simulated fault gouge caused by the combined effects of phyllosilicates and pressure solution, *Tectonophysics*, *327*(3–4), 173–194.

Brantut, N., R. Han, T. Shimamoto, N. Findling, and A. Schubnel (2011), Fast slip with inhibited temperature rise due to mineral dehydration: Evidence from experiments on gypsum, *Geology*, *39*(1), 59–62.

Brantut, N., A. Schubnel, J. N. Rouzaud, F. Brunet, and T. Shimamoto (2008), High-velocity frictional properties of a clay-bearing fault gouge and implications for earthquake mechanics, *Journal of Geophysical Research: Solid Earth*, *113*.

Bullock, R. J., N. De Paola, and R. E. Holdsworth (2015), An experimental investigation into the role of phyllosilicate content on earthquake propagation during seismic slip in carbonate faults, *Journal of Geophysical Research: Solid Earth*, *120*(5), 3187–3207.

Chester, F. M., and J. M. Logan (1987), Composite planar fabric of gouge from the Punchbowl fault, California, *Journal of Structural Geology*, *9*, 621–634.

Chester, F. M., and J. S. Chester (1998), Ultracataclasite structure and friction processes of the Punchbowl fault, San Andreas system, California, *Tectonophysics*, *295*(1–2), 199–221.

Chester, F. M., M. Friedman, and J. M. Logan (1985), Foliated cataclasites, *Tectonophysics*, *111*(1–2), 139–146.

Cladouhos, T. T. (1999), A kinematic model for deformation within brittle shear zones, *Journal of Structural Geology*, *21*(4), 437–448.

Collettini, C., and R. E. Holdsworth (2004), Fault zone weakening and character of slip along low-angle normal faults: Insights from the Zuccale fault, Elba, Italy, *Journal of the Geological Society*, *161*, 1039–1051.

Collettini, C., C. Viti, S. A. F. Smith, and R. E. Holdsworth (2009), Development of interconnected talc networks and weakening of continental low-angle normal faults, *Geology*, *37*(6), 567–570.

Cowan, D. S. (1999), Do faults preserve a record of seismic slip? A field geologist's opinion, *Journal of Structural Geology*, *21*(8–9), 995–1001.

Cowan, D. S., and M. T. Brandon (1994), A symmetry-based method for kinematic analysis of large-slip brittle fault zones, *American Journal of Science*, *294*(3), 257–306.

Cowan, D. S., T. T. Cladouhos, and J. K. Morgan (2003), Structural geology and kinematic history of rocks formed along low-angle normal faults, Death Valley, California, *Geological Society of America Bulletin*, *115*(10), 1230–1248.

De Paola, N., T. Hirose, T. Mitchell, G. Di Toro, C. Viti, and T. Shimamoto (2011), Fault lubrication and earthquake propagation in thermally unstable rocks, *Geology*, *39*(1), 35–38.

De Paola, N., R. E. Holdsworth, C. Viti, C. Collettini, and R. J. Bullock (2015), Can grain size sensitive flow lubricate faults during the initial stages ofearthquake propagation? *Earth and Planetary Science Letters*, *431*, 48–58.

Delle Piane, C., L. Burlini, and K. Kunze (2009), The influence of dolomite on the plastic flow of calcite rheological, microstructural and chemical evolution during large strain torsion experiments, *Tectonophysics*, *467*(1–4), 145.

Di Toro, G., A. Niemeijer, A. Tripoli, S. Nielsen, F. Di Felice, P. Scarlato, G. Spada, R. Alessandroni, G. Romeo, G. Di Stefano, S. Smith, E. Spagnuolo, and S. Mariano (2010), From field geology to earthquake simulation: a new state-of-the-art tool to investigate rock friction during the seismic cycle (SHIVA), *Rendiconti Lincei-Scienze Fisiche E Naturali*, *21*, 95–114.

Engelder, J. T. (1974), Cataclasis and the generation of fault gouge, *Geological Society of America Bulletin*, *85*, 1515–1522.

Fabbri, O., A. M. Lin, and H. Tokushige (2000), Coeval formation of cataclasite and pseudotachylyte in a Miocene forearc granodiorite, southern Kyushu, Japan, *Journal of Structural Geology*, *22*(8), 1015–1025.

Fagereng, A. (2011), Frequency-size distribution of competent lenses in a block-in-matrix melange, Imposed length scales of brittle deformation? *Journal of Geophysical Research—Solid Earth*, *116*.

Fondriest, M., S. Aretusini, G. Di Toro, and S. A. F. Smith (2015), Fracturing and rock pulverization along an exhumed fault zone in dolostones: The Foiana Fault Zone (Southern Alps, Italy), *Tectonophysics*, 654, 56–74.

Fondriest, M., S. A. F. Smith, T. Candela, S. Nielsen, K. Mair, and G. Di Toro (2013), Mirror-like faults and power dissipation during earthquakes, *Geology*, *41*, 1175–1178.

Green, H. W., F. Shi, K. Bozhilov, G. Xia, and Z. Reches (2015), Phase transformation and nanometric flow cause extreme weakening during fault slip, *Nature Geoscience*, *8*(6), 484–491.

Griffiths, J. R. (2014), *Using earthquake-like laboratory experiments to reveal ancient seismicity in the rock record*, Bachelor of Science (with Honors), University of Otago.

Gueydan, F., Y. M. Leroy, L. Jolivet, and P. Agard (2003), Analysis of continental midcrustal strain localization induced by microfracturing and reaction-softening, *Journal of Geophysical Research: Solid Earth*, *108*(B2), 2064, doi:2010.1029/2001JB000611.

Haines, S., B. Kaproth, C. Marone, D. Saffer, and B. A. van der Pluijm (2013), Shear zones in clay–rich fault gouge: A laboratory study of fabric development and evolution, *Journal of Structural Geology*, *51*, 206–225.

Hayman, N. W., B. A. Housen, T. T. Cladouhos, and K. Livi (2004), Magnetic and clast fabrics as measurements of grain-scale processes within the Death Valley shallow crustal detachment faults, *Journal of Geophysical Research: Solid Earth*, *109*(B5), B05409, doi:05410.01029/02003JB02902.

Herwegh, M., and K. Kunze (2002), The influence of nano-scale second-phase particles on deformation of fine grained calcite mylonites, *Journal of Structural Geology*, *24*, 1463–1478.

Holdsworth, R. E. (2004), Weak faults: Rotten cores, *Science*, *303*(5655), 181–182.

Holdsworth, R. E., E. W. E. van Diggelen, C. J. Spiers, J. H. P. de Bresser, R. J. Walker, and L. Bowen (2011), Fault rocks from the SAFOD core samples: Implications for weakening at shallow depths along the San Andreas Fault, California, *Journal of Structural Geology*, *33*(2), 132–144.

Imber, J., R. E. Holdsworth, C. A. Butler, and G. E. Lloyd (1997), Fault-zone weakening processes along the reactivated Outer Hebrides Fault Zone, Scotland, *Journal of the Geological Society*, *154*, 105–109.

Jefferies, S. P., R. E. Holdsworth, C. A. J. Wibberley, T. Shimamoto, C. J. Spiers, A. R. Niemeijer, and G. E. Lloyd (2006), The nature and importance of phyllonite development in crustal-scale fault cores: An example from the Median Tectonic Line, Japan, *Journal of Structural Geology*, *28*(2), 220–235.

Kim, J. W., J. H. Ree, R. Han, and T. Shimamoto (2010), Experimental evidence for the simultaneous formation of pseudotachylyte and mylonite in the brittle regime, *Geology*, *38*(12), 1143–1146.

Kitajima, H., J. S. Chester, F. M. Chester, and T. Shimamoto (2010), High-speed friction of disaggregated ultracataclasite in rotary shear: Characterization of frictional heating, mechanical behavior, and microstructure evolution, *Journal of Geophysical Research: Solid Earth*, *115*.

Lin, A. M. (2001), S-C fabrics developed in cataclastic rocks from the Nojima fault zone, Japan and their implications for tectonic history, *Journal of Structural Geology*, *23*(6–7), 1167–1178.

Logan, J. M., C. A. Dengo, N. G. Higgs, and Z. Z. Wang (1992), Fabrics of experimental fault zones: Their development and relationship to mechanical behaviour, in *Fault Mechanics and Transport Properties of Rocks*, edited by B. Evans and T. F. Wong, Academic Press, London, 33–68.

Logan, J. M., M. Friedman, N. Higgs, C. Dengo, and T. Shimamoto (1979), Experimental studies of simulated gouge and their application to studies of natural fault zones, *Proceedings of Conference VIII on Analysis of Actual Fault Zones in Bedrock*, U.S. Geological Survey Open-File Report 79–1239.

Mair, K., and J. F. Hazzard (2007), Nature of stress accommodation in sheared granular material: Insights from 3D numerical modeling, *Earth and Planetary Science Letters*, *259*(3–4), 469–485.

Manatschal, G. (1999), Fluid- and reaction-assisted low-angle normal faulting: Evidence from rift-related brittle fault rocks in the Alps (Err Nappe, eastern Switzerland), *Journal of Structural Geology*, *21*(7), 777–793.

Mitchell, T. M., S. A. F. Smith, M. H. Anders, G. Di Toro, S. Nielsen, A. Cavallo, and A. D. Beard (2015), Catastrophic emplacement of giant landslides aided by thermal decomposition: Heart Mountain, Wyoming, *Earth and Planetary Science Letters*, *411*, 199–207.

Moore, D. E., and M. J. Rymer (2007), Talc-bearing serpentinite and the creeping section of the San Andreas fault, *Nature*, *448*(7155), 795–797.

Niemeijer, A., G. Di Toro, A. Griffith, A. Bistacchi, S. A. F. Smith, and S. Nielsen (2012), Inferring earthquake physics and chemistry using an integrated field and laboratory approach, *Journal of Structural Geology*, *39*, 2–36.

Niemeijer, A., G. Di Toro, S. Nielsen, and F. Di Felice (2011), Frictional melting of gabbro under extreme experimental conditions of normal stress, acceleration, and sliding velocity, *Journal of Geophysical Research: Solid Earth*, *116*.

Niemeijer, A. R., and C. J. Spiers (2006), Velocity dependence of strength and healing behaviour in simulated phyllosilicate-bearing fault gouge, *Tectonophysics*, *427*(1–4), 231–253.

Oohashi, K., T. Hirose, and T. Shimamoto (2011), Shear-induced graphitization of carbonaceous materials during

seismic fault motion: Experiments and possible implications for fault mechanics, *Journal of Structural* Geolog,y *33*(6), 1122–1134.

Proctor, B., T. M. Mitchell, G. Hirth, D. Goldsby, F. Zorzi, and G. Di Toro (2014), Dynamic weakening of serpentinite gouges and bare-surfaces at seismic slip rates, *Journal of Geophysical Research: Solid Earth*, doi:10.1002/2014JB011057.

Ree, J. H., J. I. Ando, R. Han, and T. Shimamoto (2014), Coseismic microstructures of experimental fault zones in Carrara marble, *Journal of Structural Geology*, *66*, 75–83.

Rempe, M., S. A. F. Smith, F. Ferri, T. M. Mitchell, and G. Di Toro (2014), Clast-cortex aggregates in experimental and natural calcite-bearing fault zones, *Journal of Structural Geology*, *68*, 142–157.

Rutter, E. H., R. E. Holdsworth, and R. J. Knipe (2001), The nature and tectonic significance of fault-zone weakening: An introduction, *Nature and Tectonic Significance of Fault Zone Weakening*, 186, 1–11.

Rutter, E. H., R. H. Maddock, S. H. Hall, and S. H. White (1986), Comparitive microstructures of natural and experimentally produced clay-bearing fault gouges, *Pure and Applied Geophysics*, *124*, 3–30.

Sagy, A., and E. Brodsky (2009), Geometric and rheological asperities in an exposed fault zone, *Journal of Geophysical Research*, *114*, B02301, doi:02310.01029/02008JB005701.

Sammis, C. G., and Y. Ben-Zion (2008), Mechanics of grain-size reduction in fault zones, *Journal of Geophysical Research: Solid Earth*, *113*(B2), doi:10.1029/2006JB004892.

Samtani, M., D. Dollimore, and K. S. Alexander (2002), Comparison of dolomite decomposition kinetics with related carbonates and the effect of procedural variables on its kinetic parameters, *Thermochimica Acta*, *392*, 135–145.

Sawai, M., T. Shimamoto, and T. Togo (2012), Reduction in BET surface area of Nojima fault gouge with seismic slip and its implication for the fracture energy of earthquakes, *Journal of Structural Geology*, *38*, 117–138.

Sibson, R. H. (1977), Fault rocks and fault mechanisms, *Journal of the Geological Society, London*, *133*, 191–213.

Sibson, R. H. (2003), Thickness of the seismic slip zone, *Bulletin of the Seismological Society of America*, *93*(3), 1169–1178.

Smith, S. A. F., G. Di Toro, S. Kim, J. H. Ree, S. Nielsen, A. Billi, and R. Spiess (2013), Co-seismic recrystallization during shallow earthquake slip, *Geology*, *41*(1), 63–66.

Smith, S. A. F., S. Nielsen, and G. Di Toro (2015), Strain localization and the onset of dynamic weakening in calcite fault gouge, *Earth and Planetary Science Letters*, *413*, 25–36.

Snoke, A. W., J. Tullis, and V. R. Todd (1998), *Fault-Related Rocks: A Photographic Atlas*, Princeton University Press.

Stewart, M., R. E. Holdsworth, and R. A. Strachan (2000), Deformation processes and weakening mechanisms within the frictional-viscous transition zone of major crustal-scale faults: Insights from the Great Glen Fault Zone, Scotland, *Journal of Structural Geology*, *22*(5), 543–560.

Stirling, M., T. Goded, K. Berryman, and N. Litchfield (2013), Selection of earthquake scaling relationships for seismic-hazard analysis, *Bulletin of the Seismological Society of America*, *103*(6), 2993–3011.

Tanaka, H. (1992), Cataclastic lineations, *Journal of Structural Geology*, *14*(10), 1239–1252.

Togo, T. and T. Shimamoto (2012), Energy partition for grain crushing in quartz gouge during subseismic to seismic fault motion: An experimental study. *Journal of Structural Geology 38*, 139–155.

Wallis, D., G. E. Lloyd, R. J. Phillips, A. J. Parsons, and R. D. Walshaw (2015), Low effective fault strength due to frictional-viscous flow in phyllonites, Karakoram fault zone, NW India, *Journal of Structural Geology*, *77*, 45–61.

Wallis, D., R. J. Phillips, and G. E. Lloyd (2013), Fault weakening across the frictional-viscous transition zone, Karakoram fault zone, NW Himalaya, *Tectonics*, *32*(5), 1227–1246.

White, S. R. (2001), Textural and microstructural evidence for semi-brittle flow in natural fault rocks with varied mica contents, *International Journal of Earth Sciences*, *90*(1), 14–27.

Wintsch, R. P., R. Christoffersen, and A. K. Kronenberg (1995), Fluid-rock reaction weakening of fault zones, *Journal of Geophysical Research: Solid Earth*, *100*(B7), 13021–13032.

Wintsch, R. P., and K. Yi (2002), Dissolution and replacement creep: A significant deformation mechanism in mid-crustal rocks, *Journal of Structural Geology*, *24*(6–7), 1179–1193.

Yao, L., S. L. Ma, T. Shimamoto, and T. Togo (2013), Structures and high-velocity frictional properties of the Pingxi fault zone in the Longmenshan fault system, Sichuan, China, activated during the 2008 Wenchuan earthquake, *Tectonophysics*, *599*, 135–156.